Wind work at the air-sea interface: A Modeling Study in Anticipation of Future Space Missions

Hector S. Torres[1], Patrice Klein[1,2,3], Jinbo Wang[1], Alexander Wineteer[1], Bo Qiu[4], Andrew F. Thompson[2], Lionel Renault[8], Ernesto Rodriguez[1], Dimitris Menemenlis[1], Andrea Molod[5], Christopher N. Hill[6], Ehud Strobach[7], Hong Zhang[1], Mar Flexas[2], and Dragana Perkovic-Martin[1]

[1]Jet Propulsion Laboratory, California Institute of Technology, Pasadena, CA, USA
[2]Environmental Science and Engineering, California Institute of Technology, Pasadena, CA, USA
[3]LMD/IPSL, CNRS, Ecole Normale Supérieure, PSL Research University, 75005 Paris, France
[4]University of Hawaii, Honolulu, HI, USA
[5]NASA Goddard Space Flight Center, MD, USA
[6]Earth, Atmospheric and Planetary Sciences, Massachusetts Institute of Technology, MA, USA
[7]Agricultural Research Organization, Israel
[8]LEGOS, University of Toulouse, IRD, CNRS, CNES, UPS, Toulouse, France

Correspondence: Hector S. Torres (Hector.Torres.Gutierrez@jpl.nasa.gov)

Abstract. Wind work at the air-sea interface is the transfer of kinetic energy between the ocean and the atmosphere and, as such, is an important part of the atmosphere-ocean coupled system. Wind work is defined as the scalar product of ocean wind stress and surface current, with each of these two variables spanning, in this study, a broad range of spatial and temporal scales, from 10 km to more than 3000 km and hours to months. These characteristics emphasize wind work's multi-scale nature. In the absence of appropriate global observations, our study makes use of a new, global, coupled ocean-atmosphere simulation, with horizontal grid spacing of 2–5 km for the ocean and 7 km for the atmosphere, analyzed for 12 months. We develop a methodology, both in physical and spectral spaces, to diagnose three different components of wind work that force distinct classes of ocean motions, including high-frequency internal gravity waves such as near-inertial oscillations, low-frequency currents such as those associated with eddies, and seasonally averaged currents, such as zonal tropical and equatorial jets. The total wind work, integrated globally, has a magnitude close to 5 TW, a value that matches recent estimates. Each of the first two components, that force high and low-frequency currents, accounts for ∼28% of the total wind work and the third one, that forces seasonally averaged currents, ∼44%. These three components, when integrated globally, weakly vary with seasons, but their spatial distribution over the oceans has strong seasonal and latitudinal variations. In addition, the high-frequency component, that forces internal gravity waves, is highly sensitive to the collocation in space and time (at scales of a few hours) of wind stresses and ocean currents. Furthermore, the low-frequency wind work component acts to damp currents with a size smaller than 250 km and strengthen currents with larger sizes. This emphasizes the need to perform a full kinetic budget involving the wind work and nonlinear advection terms since small and larger-scale low-frequency currents interact through these nonlinear terms. The complex interplay of surface wind stresses and currents revealed by the numerical simulation motivates the need for winds-and-currents satellite missions to directly observe wind work.

1   Introduction

Wind work is known to drive a large part of ocean dynamics (Ferrari and Wunsch, 2009), and is defined in this study as the scalar product of the wind stress and surface ocean current vectors (Renault et al., 2016; Yu et al., 2018). Wind work forces zonal jets (spatial scales of $\sim$1000 km and time scales of days to months), in particular at equatorial and tropical latitudes,

25 where they are key players in the El Niño Southern Oscillation (ENSO) (Maximenko et al., 2005). Wind work also forces or damps mid-latitude currents (with spatial scales from 10 km to more than 500 km and time scales of days to months), such as those associated with submesoscale, and mesoscale eddies, which are critical players in the horizontal and vertical transport of heat at these latitudes (Eden and Dietze, 2009; Zhai et al., 2012; Zhai, 2013; Klein et al., 2019; Rai et al., 2021). Additionally, wind work generates near-inertial oscillations and internal gravity waves (spatial scales of 10 to 1000 km and time scales of

30 hours), which impact mixing in the ocean interior and therefore contribute to setting the structure and strength of the Meridional Overturning Circulation (MOC) (Komori et al., 2008; Polzin and Lvov, 2011; Nikurashin et al., 2013; Alford et al., 2016).

To better identify the nonlinearities and spatial and temporal scales that characterize wind work, let us examine the dynamical variables involved. The wind stress vector, $\boldsymbol{\tau}$, can be written as (Large and Yeager, 2004)

35 $$\boldsymbol{\tau} = \rho_{air} C_d |\mathbf{U_a} - \mathbf{u_o}|(\mathbf{U_a} - \mathbf{u_o}), \tag{1}$$

where ρ_{air} is the air density, and C_d a drag coefficient that is a function of the wind field and stability of the atmospheric boundary layer (see next section). $\mathbf{U_a}$ is the vector wind usually taken at an altitude of 10 m, and $\mathbf{u_o}$ the ocean-surface current vector. Then the wind work, F_s, is

$$F_s = \boldsymbol{\tau} \cdot \mathbf{u_o} = \rho_{air} C_d |\mathbf{U_a} - \mathbf{u_o}|(\mathbf{U_a} - \mathbf{u_o}) \cdot \mathbf{u_o} \tag{2}$$

40 Eq. 2 highlights that wind work is nonlinearly related to wind stress and ocean current.

Referring to Eq.2, some examples of the multiscale issues we have to address are the following. Wind fluctuations with time scales of one hour impact the wind stress at these short time scales. The resulting wind work, in regions of atmospheric storm tracks, generates near-inertial motions and internal gravity waves (with time scales less than a day) whose kinetic energy can

45 be up to twice larger than when only wind fluctuations with time scales longer than six hours are considered (Klein et al., 2004; Rimac et al., 2013). However, wind fluctuations at short time scales also impact the weekly-averaged and monthly-averaged wind stress and therefore the wind work at these longer time scales. This is due to the quadratic relationship between winds and wind stress (Eq. 1). For example, in regions of atmospheric storm tracks, the resulting monthly-averaged wind work is larger by a factor four when wind fluctuations at short time scales are taken into account than when only weekly or monthly

50 winds are used (Zhai et al., 2012; Zhai, 2017). Thus, high-frequency winds can lead to a larger forcing of low-frequency ocean

currents. This example and the more detailed arguments developed in Section 3 emphasize the need to have observations of winds and currents over a broad range of temporal and spatial scales in order to diagnose the different wind work components that energize or damp oceanic motions.

55 To assess the broad range of scales that influence wind work and impact ocean currents, we make use of model outputs of wind stresses and ocean currents from a new, global, coupled ocean-atmosphere model that includes tidal forcing in the ocean and has horizontal grid spacing of 2–5 km in the ocean and 7 km in the atmosphere. This model has been integrated for more than a year. The resulting numerical simulation produces wind and current fluctuations at very short time scales (45-s ocean-atmosphere coupling time step), enables spatial collocation and contemporaneity of atmospheric winds and ocean currents, and

60 takes into account the impacts of winds and ocean currents on wind stresses. Our study focuses on the impact of wind work on ocean currents including near-inertial oscillations, mesoscale eddies, large-scale currents and gyres, but does not account for high frequency motions such as surface gravity waves, Langmuir circulation, and mixed layer turbulence. The next section describes the global numerical model used. Section 3 describes the methodology employed in physical and spectral spaces, and discusses the multiscale issues we have to address. An analysis of the wind work components that force different classes

65 of motion is presented in Section 4. Conclusions follow in Section 5.

2 Numerical simulation of the coupled ocean-atmosphere system

The new, global, Coupled Ocean-Atmosphere Simulation (COAS) used in this study comprises the Goddard Earth Observing System (GEOS) atmospheric and land model coupled to an ocean configuration of the Massachusetts Institute of Technology

70 general circulation model (MITgcm). The configuration of COAS used in this study is identical to that used in the studies of Strobach et al. (2020, 2022) except that the ocean model includes tidal forcing, which triggers the generation of internal tides and promotes a more realistic internal gravity wave continuum.

The GEOS model was configured to use the C1440 cubed-sphere grid, which has nominal horizontal grid spacing of 6.9 km.

75 The vertical grid type is hybrid sigma-pressure with 72 levels. A detailed description of the GEOS atmospheric model configuration used in COAS is found in Molod et al. (2015) and Strobach et al. (2020). The surface layer parameterisation of turbulent fluxes is a modified version of the parameterisation documented in Helfand and Schubert (1995), with a wind stress and surface roughness model modified by the updates of Garfinkel et al. (2011) for a mid-range of wind speeds, and further modified by the updates of Molod et al. (2013) for high winds.

80

The MITgcm component of COAS uses the Latitude-Longitude-polar-Cap 2160 (LLC2160) configuration described in Arbic et al. (2018) and previously used in the studies of Flexas et al. (2019), Su et al. (2018), and many others. The LLC2160 solves the hydrostatic primitive equations for velocity, potential temperature, and salinity with a seawater equation of state. The finite

volume method is used to discretize the equations in space. The LLC2160 configuration uses an implicit free surface, real freshwater surface forcing, and the K-Profile Parameterization (KPP) vertical mixing scheme of Large et al. (1994) but with the non-local term disabled. The LLC2160 has nominal horizontal grid spacing of 1/24°, ranging from 2.3 km in the Arctic Ocean, 4.6 km at the Equator, and 1.7 km at the southernmost location around Antarctica. There are 90 vertical levels with 1-m vertical grid spacing at the surface, gradually increasing to ~300 m near the 5000-m depth. The integration time step for the GEOS C1440 and the MITgcm LLC2160 components and the coupling time step for the coupled C1440-LLC2160 COAS model is 45 seconds.

The formalism of the coupling between the atmosphere and the ocean is classical and can be explained as follows. The Monin-Obukhov similarity theory-based parameterization of surface layer turbulence used to compute air/sea fluxes of heat, moisture and momentum is described in Helfand and Schubert (1995). This parameterization includes the effects of a viscous sublayer over oceans based on Yaglom and Kader (1974), which describes a resistance to enthalpy transfer that increases with surface roughness. The stability functions for unstable surface layers are the KEYPS equation of Panofsky et al. (1977) for momentum and its generalization for scalar quantities. For stable surface layers the stability functions are those of Clarke (1970) for momentum and heat. The ocean roughness is determined by a polynomial which is a blend of the algorithms of Large and Pond (1981) and Kondo (1975) for low wind speeds, modified in the mid-range wind regime based on recent observations in the Southern Ocean according to Garfinkel et al. (2011) and in the high wind regime according to Molod et al. (2013). Note that the ocean and atmosphere exchange momentum, heat, and fresh water through a "skin layer" interface which includes a parameterization of the diurnal cycle (Price et al., 1978). For the high-resolution simulation discussed here, the inertia of the skin layer is small. Finally, computations of momentum and heat fluxes at the air-sea interface take into account the differences between ocean and atmosphere resolutions. This is done using an exchange grid, created by the intersection of the ocean and atmospheric grids, which ensures complete conservation of momentum, heat, and freshwater flux across the air-sea interface.

The COAS simulation was initialized on January 20 using 2012 ocean initial conditions from the forced LLC2160 MITgcm simulation and 2020 atmospheric initial conditions from the Modern-Era Retrospective analysis for Research and Applications, Version 2 (MERRA-2) interpolated to the C1440 GEOS grid. The reason for using 2012 ocean initial conditions is that there was no other spun-up MITgcm simulation of sufficient resolution available at the time the coupled simulation began. The 2020 atmospheric initial conditions were imposed by the DYnamics of the Atmospheric general circulation Modeled On Non-hydrostatic Domains (DYAMOND; Stevens et al., 2019) Phase II protocol. The mismatch in ocean and atmospheric initial condition years is not ideal but given that this is an unconstrained coupled simulation, the simulation year is notional. The results shown in this study are based on a simulation period of 14 months (January 20, 2020 to March 25, 2021). We did not take into account the first two months that correspond to the spin-up period. Model outputs concern the last 12 months and include hourly three-dimensional fields for all oceanic and atmospheric variables, some higher-frequency (15-minute) two-dimensional atmospheric fields, and many diagnostic variables, for a total storage requirement of ~2 Petabytes.
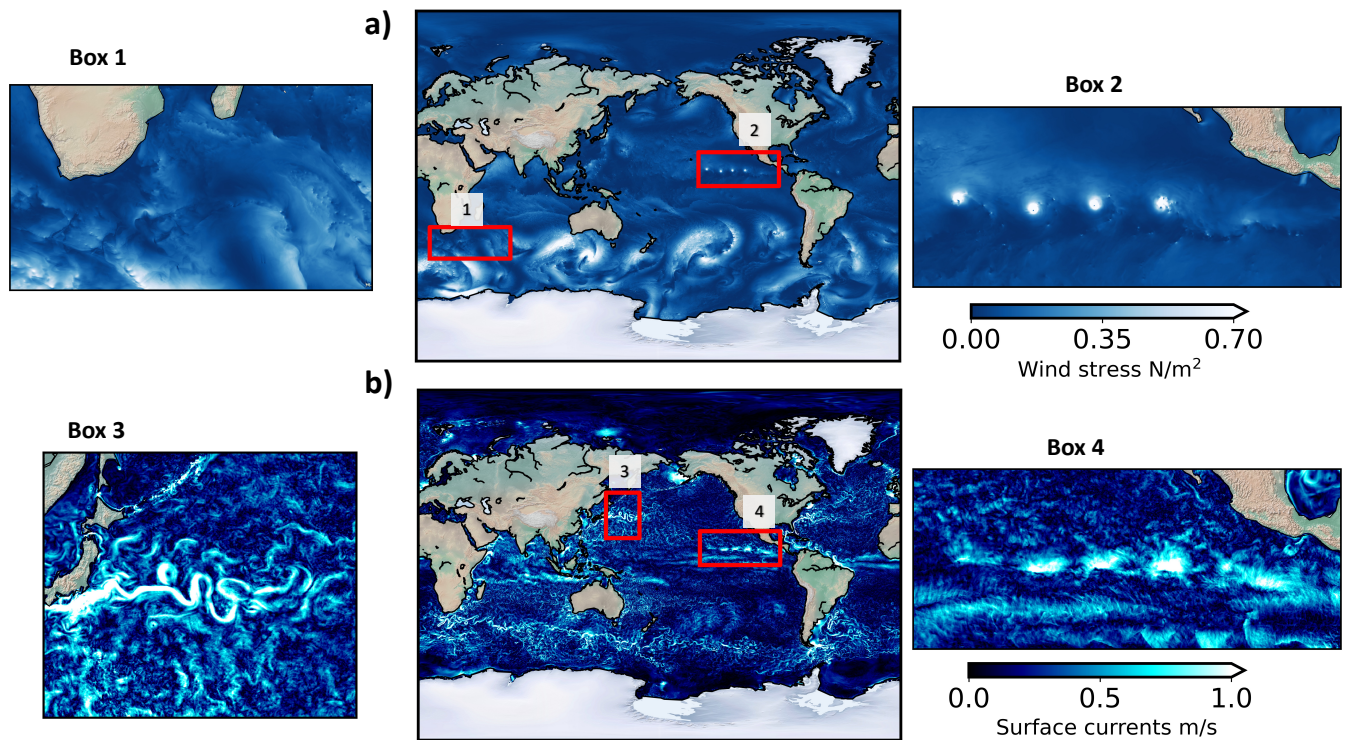
Figure 1. (a) Snapshots of surface wind stress and (b) ocean-surface currents in the Coupled Ocean-Atmosphere Simulation (COAS) in July 22, 12:00 GMT.

3 Methodology in physical and spectral spaces

3.1 Wind stresses and ocean currents in physical space

Outputs of wind stress and ocean current from the coupled simulation are decomposed into different components based on temporal and spatial scales, with this decomposition based on the time and spatial variability of winds and currents.

Figures 1a and b show a snapshot of wind stresses and ocean currents in the global ocean. Movies of these two key variables are available in https://doi.org/10.5281/zenodo.6478679. The wind stress variations have large scales, $\mathcal{O}(1000\,\text{km})$ (Figure 1a), resulting from atmospheric weather patterns that propagate rapidly, for example, going from South Africa to South America within 6–10 days (Figure 1a). Embedded within these large-scale patterns are smaller-scale patterns (as small as 100 km), some of them propagating with the large-scale ones, others being quasi-stationary (see Box 1 on Figure 1a and the movie). The latter are mostly the signature of ocean currents on the wind stress and can be identified from watching the movie. Impact of land topography on the wind stress is also noticeable in the movies, in particular close to the east coast of Asia at mid-latitudes and the west coast of Mexico at the equator. The latter may lead to the formation of hurricanes, such as those noticeable in Box
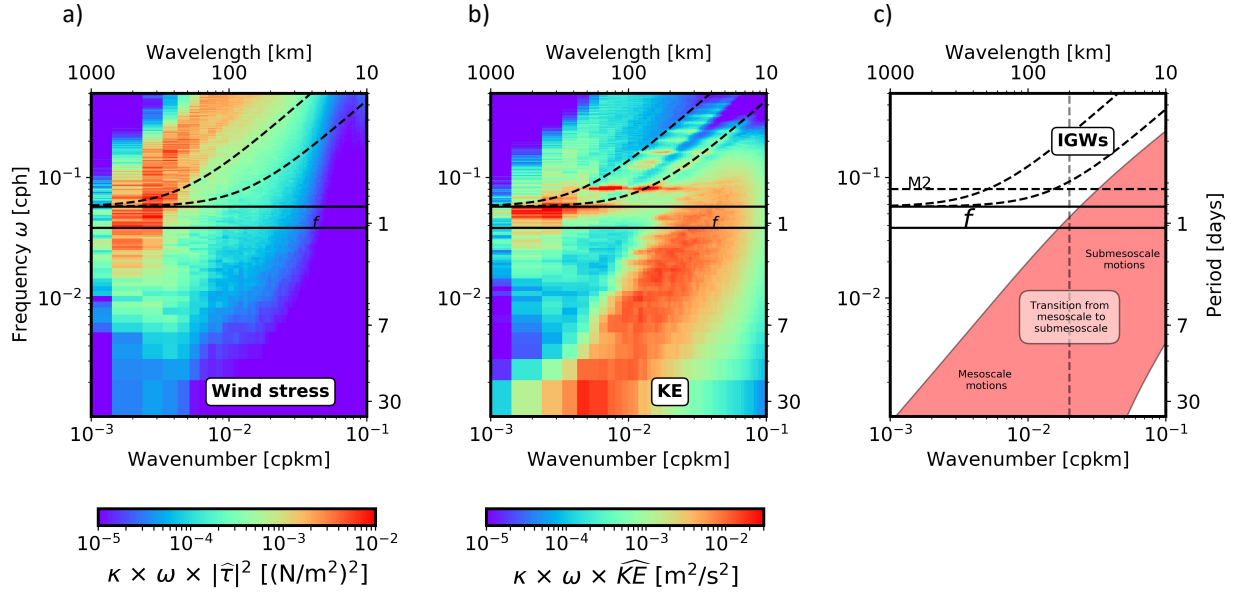
Figure 2. COAS frequency-wavenumber spectra of (a) surface wind stress and (b) surface currents in the Kuroshio Extension region in winter. Panel (c) is a Stommel Diagram of oceanic motions (see text). The dashed lines in the three panels show the linear dispersion relation curves for internal gravity waves associated with the first four baroclinic modes, which helps to identify energetic internal gravity waves. See Torres et al. (2018) and Qiu et al. (2018) for a detailed explanation of the above partition.

2 of Figure 1a. Energetic ocean currents (Figure 1b) are characterized by very small scales in contrast to the wind stress and move slowly as revealed by the movie (see also Box 3 on Figure 1b). These motions are mostly associated with wavy/unstable baroclinic mean currents and eddies. Zonal jets are noticeable at the equator and in tropical regions (Figure 1b). Not surprisingly, hurricanes have a strong signature on surface currents (Box 4 on Figure 1b). Ocean current patterns with larger scales, but containing less energy than small-scale currents, are also noticeable in the movie. These patterns propagate with large-scale atmospheric storms. They are the signature of near-inertial motions and internal waves driven by the large-scale winds stress.

3.2 Wind stresses and ocean currents in spectral space

The different temporal and spatial scales of wind stresses and ocean currents are further characterized in spectral space in regional domains. Figure 2 shows spectra of wind stresses and currents in the Kuroshio Extension region in the North Pacific (see Appendix A for spectra calculation details). The frequency and wavenumber ranges span, respectively, periods between 2 hours and 40 days and length scales from 10 km to 1000 km. Wind stresses and currents occupy different regions in spectral space. On the one hand, wind stresses (Figure 2a) are mostly characterized by high frequencies (< 2 days) comprised of large spatial scales (>500 km) for time scales larger than 12 hours and small spatial scales (20–500 km) for time scales smaller

than 12 hours. Such wind stresses are the signature of large-scale atmospheric storms and the associated small-scale patterns that propagate with them. Small-scale wind stress patterns associated with slowly-moving ocean eddies are weaker and occupy periods larger than 2 days. On the other hand, energetic ocean currents (Figure 2b) are mostly characterized by smaller spatial scales (<500 km) and lower frequencies (periods >2 days). As sketched in Figure 2c, these currents are associated with mesoscale eddies known to be driven by the baroclinic instability of mean currents. However, ocean currents also have a large magnitude in the near-inertial band ($\omega \approx f$) with scales larger than 500 km. These currents are associated with near-inertial waves (see Figure 2c) forced by high-frequency winds.

Based on the properties discussed above, we analysed the wind work over a three-month period, during winter, spring, summer and fall to emphasize its seasonality. During each season, we consider the following decomposition for surface wind stress $\boldsymbol{\tau}$ and ocean-surface currents $\mathbf{u_o}$:

$$\mathbf{X} = \overline{\mathbf{X}} + \mathbf{X}'_{hf} + \mathbf{X}'_{lf>} + \mathbf{X}'_{lf<} \, , \tag{3}$$

where $\mathbf{X}$ represents either $\boldsymbol{\tau}$ or $\mathbf{u_o}$, the overline operator represents a time-average over 3 months, also called time-mean or seasonal-mean, and the prime operator represents time fluctuations with periods smaller than 3 months. The time fluctuations are further decomposed into a high-frequency component (hf) for periods smaller than 3 days and a low-frequency component (lf) for periods between 3 days and 3 months. Varying the 3-day threshold between low-frequency and high-frequency motions does not have a significant impact on the results of the present study. The hf component captures high-frequency contributions such as those at the inertial frequency. The low-frequency component is further decomposed into two contributions in terms of spatial scales: the large-scale contribution ($lf>$) for spatial scales larger than a critical length scale L_c and the small-scale contribution ($lf<$) for scales smaller than L_c. Following Rai et al. (2021), we define L_c as the length scale for which the low-frequency component of wind work is negative for scales smaller than L_c and positive for larger scales. Negative wind work at these scales has been referred to as "eddy killer" or "eddy damping", a mechanism that has been thoroughly investigated during the past 15 years (Eden and Dietze, 2009; Renault et al., 2016, 2018; Rai et al., 2021). Using the same procedure as Rai et al. (2021), we found that $L_c \approx 250$ km (see Section 4.3 for more details).

3.3 Analysis of the wind work

The wind work depends not only on the amplitudes of time-mean and fluctuating surface wind stress and currents but also on their cross-correlation. We apply the Reynolds decomposition to Eq. 2 using Eq. 3. The resulting wind work at each grid point averaged over 3 months includes a time-mean component ($\overline{\boldsymbol{\tau}}.\overline{\mathbf{u_o}}$) and a total time-dependent component ($\overline{\boldsymbol{\tau}'.\mathbf{u_o}'} = \overline{\boldsymbol{\tau}'_{hf}.\mathbf{u_o}'_{hf}} + \overline{\boldsymbol{\tau}'_{lf>}.\mathbf{u_o}'_{lf>}} + \overline{\boldsymbol{\tau}'_{lf<}.\mathbf{u_o}'_{lf<}}$), such that

$$\overline{F_s} = \overline{\boldsymbol{\tau}}.\overline{\mathbf{u_o}} + \overline{\boldsymbol{\tau}'_{hf}.\mathbf{u_o}'_{hf}} + \overline{\boldsymbol{\tau}'_{lf>}.\mathbf{u_o}'_{lf>}} + \overline{\boldsymbol{\tau}'_{lf<}.\mathbf{u_o}'_{lf<}} \, . \tag{4}$$

First, we have checked the validity of the Reynolds decomposition by estimating the order of magnitude of each cross term not present in Eq. 4. Their order of magnitude is 10^{-6} smaller than the terms present in Eq. 4 (compare Figure 3 with Figure 4 and
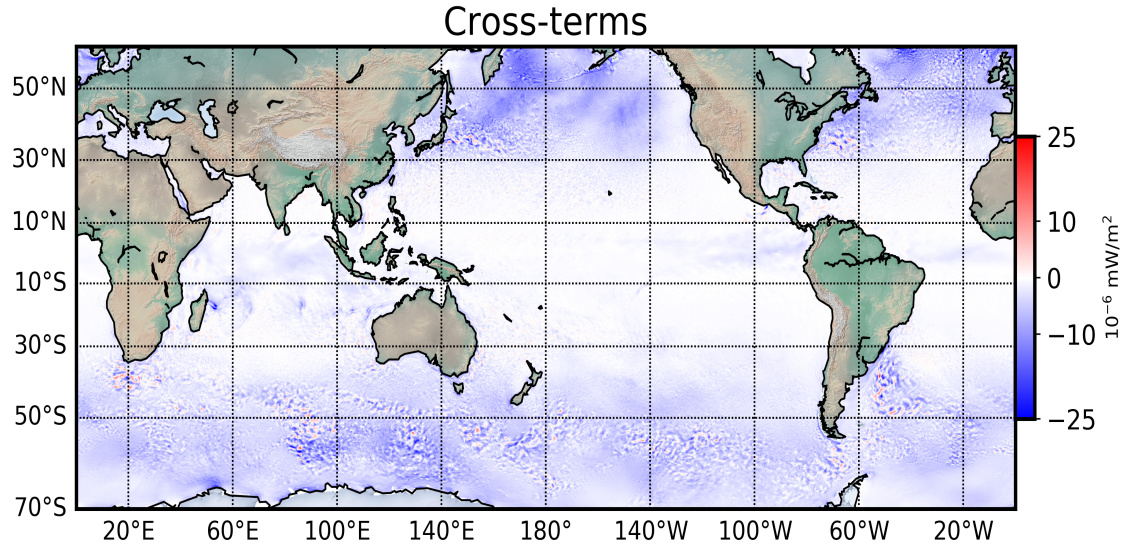
Figure 3. The cross terms not present in Eq. 4 estimated as the differences between the left and right hand sides of this equation

others), which confirms the pertinence of our decomposition. Estimation of these cross terms is consistent with the estimation found by Renault et al. (2020). The four terms on the right hand side (RHS) of Eq. 4 identify the contribution of the different

180 time and spatial scales of the wind stress and current to the wind work averaged over three months. Each term in Eq. 4, associated with a given class of temporal and spatial fluctuations, directly forces surface currents corresponding to the same class as explained in Appendix B. Thus, the first term on the right hand side (RHS) in Eq. 4 should force mean currents ($\overline{\mathbf{u}}_\mathbf{o}$), the second one, mostly near-inertial waves and internal gravity waves ($\mathbf{u}_{\mathbf{o}hf}^{'}$), the third one, large-scale currents and gyres ($\mathbf{u}_{\mathbf{o}lf>}^{'}$), and the last one, mesoscale eddies ($\mathbf{u}_{\mathbf{o}lf<}^{'}$).

185

However, each class of motions can be indirectly forced by the wind work associated with other time and spatial scales. This is due to the presence of the nonlinear advection terms in the momentum equations (see also Appendix B). Let us consider for example the equations for the time evolution of $\mathbf{u}_{\mathbf{o}lf<}^{'}$ and $\mathbf{u}_{\mathbf{o}lf>}^{'}$ where only nonlinear advection terms related to $\mathbf{u}_{\mathbf{o}lf<}^{'}$ and $\mathbf{u}_{\mathbf{o}lf>}^{'}$ are retained for the sake of simplicity (see Eq. B14 in Appendix B for a generalization,)

$$190 \quad \frac{\partial \overline{\mathbf{u}_{\mathbf{o}lf<}^{'2}}/2}{\partial t} \sim -\overline{\mathbf{u}_{\mathbf{o}lf<}^{'}.\mathbf{u}_{\mathbf{o}lf<}^{'}.\nabla\mathbf{u}_{\mathbf{o}lf>}^{'}} - \overline{\mathbf{u}_{\mathbf{o}lf<}^{'}.\mathbf{u}_{\mathbf{o}lf<}^{'}.\nabla\mathbf{u}_{\mathbf{o}lf<}^{'}} - \overline{\mathbf{u}_{\mathbf{o}lf>}^{'}.\mathbf{u}_{\mathbf{o}lf<}^{'}.\nabla\mathbf{u}_{\mathbf{o}lf<}^{'}} + \frac{\overline{\tau_{lf<}^{'}.\mathbf{u}_{\mathbf{o}lf<}^{'}}}{H} \ , \quad (5)$$

$$\frac{\partial \overline{\mathbf{u}_{\mathbf{o}lf>}^{'2}}/2}{\partial t} \sim -\overline{\mathbf{u}_{\mathbf{o}lf>}^{'}.\mathbf{u}_{\mathbf{o}lf>}^{'}.\nabla\mathbf{u}_{\mathbf{o}lf>}^{'}} - \overline{\mathbf{u}_{\mathbf{o}lf>}^{'}.\mathbf{u}_{\mathbf{o}lf<}^{'}.\nabla\mathbf{u}_{\mathbf{o}lf<}^{'}} + \frac{\overline{\tau_{lf>}^{'}.\mathbf{u}_{\mathbf{o}lf>}^{'}}}{H} \ . \quad (6)$$

H is a mixed-layer depth assumed to be constant. From Eq. 5, surface currents, $\mathbf{u}_{\mathbf{o}lf<}^{'}$, are directly forced by $\tau_{lf<}^{'}.\mathbf{u}_{\mathbf{o}lf<}^{'}$. However, these currents are also affected by the first RHS term in Eq. 5 that involves $\mathbf{u}_{\mathbf{o}lf>}^{'}$. If currents, $\mathbf{u}_{\mathbf{o}lf>}^{'}$, are unstable, production of surface currents at smaller spatial scales ($\mathbf{u}_{\mathbf{o}lf<}^{'}$) can occur through this first RHS term. From Eq. 6, $\mathbf{u}_{\mathbf{o}lf>}^{'}$ is

195 directly forced by $\tau_{lf>}^{'}.\mathbf{u}_{\mathbf{o}lf>}^{'}$. The consequence is that, through the first RHS term in Eq.5, $\mathbf{u}_{\mathbf{o}lf<}^{'}$ is indirectly forced by

Table 1. Contributions to the wind work of the time-mean (TM) component (first term on the RHS of Eq. 4) and total time-dependent (TD) component (last three terms on the RHS of Eq. 4) from COAS, over the World ocean, in terms of seasons: January-February-March (JFM), April-May-June (AMJ), July-August-September (JAS), and October-November-December (OND). Units are TeraWatts, TW

Season	COAS total	COAS TM	COAS TD
JFM	5.54	2.5	3.04
AMJ	4.9	2.1	2.8
JAS	5.7	2.5	3.2
OND	5.55	2.25	3.3

$\tau'_{lf>}.\mathbf{u_o}'_{lf>}$. Of course, scale interactions are more complex and involve more frequencies and spatial scales as discussed at the end of Appendix B (see Eq. B14). Such nonlinear interactions enable the kinetic energy transfer between scales (inverse and direct kinetic energy cascades) as well as current instabilities. However, the present example illustrates that, in order to understand the wind impact on the ocean dynamics, we need to consider the different components of the wind work displayed in Eq. 4 altogether, and not just focusing on one or two components. The present study analyzes all wind work components. A more thorough future study should be dedicated to the kinetic energy budget in the upper oceanic layers that involves both wind work forcing and nonlinear advection of momentum.

4   Multiscale decomposition of wind work

In this section we analyse the time-mean component of the wind work (first term on the RHS of Eq. 4) as well as the total time-dependent components (the last three terms on the RHS of Eq. 4). The total time-dependent components include the high-frequency component and low-frequency component (see Eq. 4). From Table 1, time-mean (COAS TM) and total time-dependent (COAS TD) components represent respectively ∼44% and ∼56% of the total wind work. Their relative contributions as well as the total wind work (COAS total) weakly varying with seasons. The total wind work is larger than 5 TW, a value close to recent estimations (Yu et al., 2018; Yu and Metzger, 2019). However, the spatial distribution of the different wind work components vary with seasons, as discussed in the following subsections.

4.1   Time-mean component: $\overline{\tau}.\overline{\mathbf{u}}_o$

Figures 4a–d and e display a significant seasonality of the time-mean component in each hemisphere, with the wind work intensified in fall and winter as compared to spring and summer, except at mid-latitudes in the southern hemisphere. The wind work, when zonally integrated at different latitudes (Figure 4e), reach peak values of 2–2.5 GW in winter and 0.5 GW in
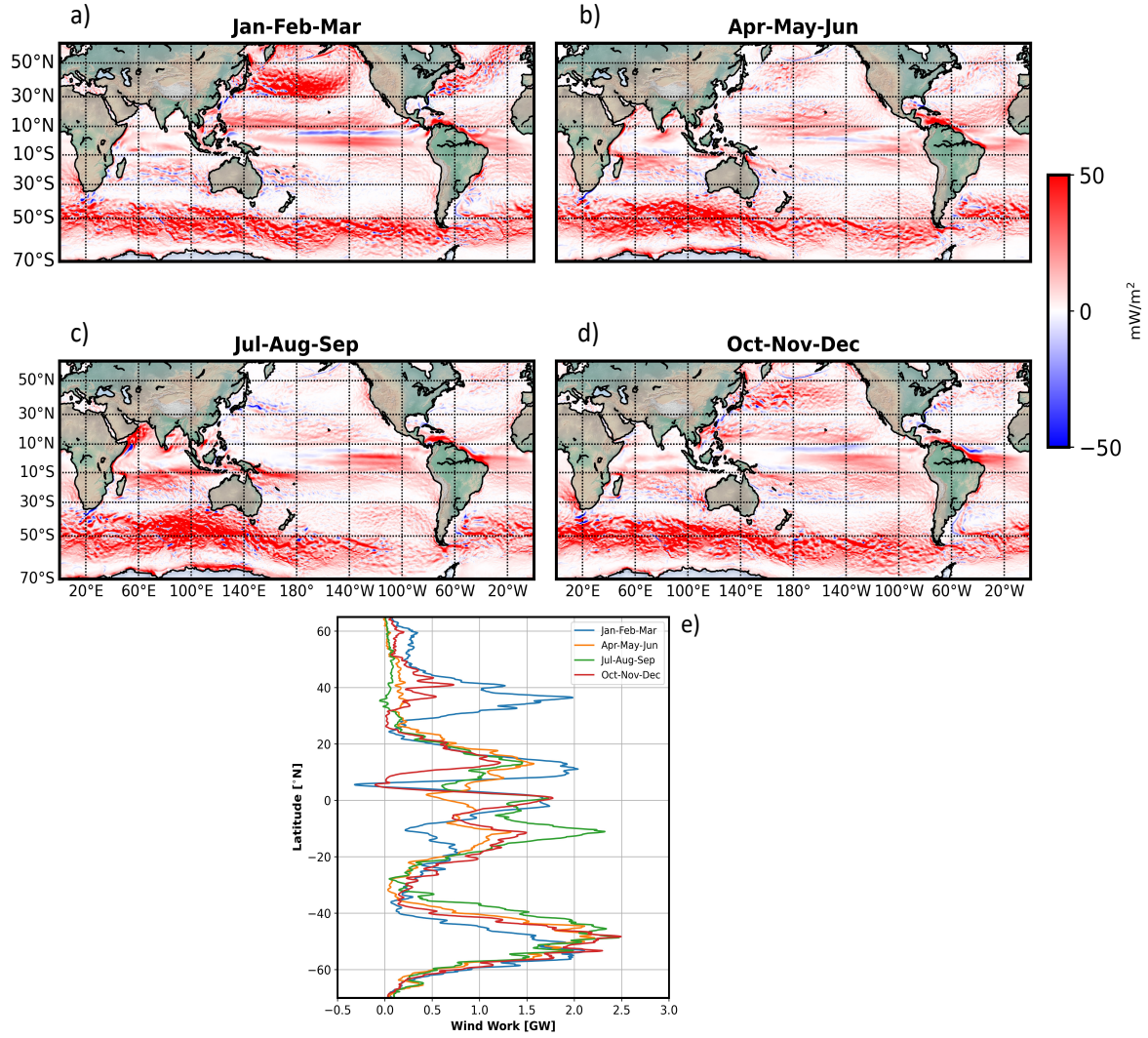
Figure 4. (a)–(d): Time-mean component of the wind work, $\overline{\tau}\cdot\overline{\mathbf{u}}_{\mathbf{o}}$, at different seasons. (e): wind work multiplied by the area of the numerical grid-cell (m^2) and zonally integrated during four seasons.
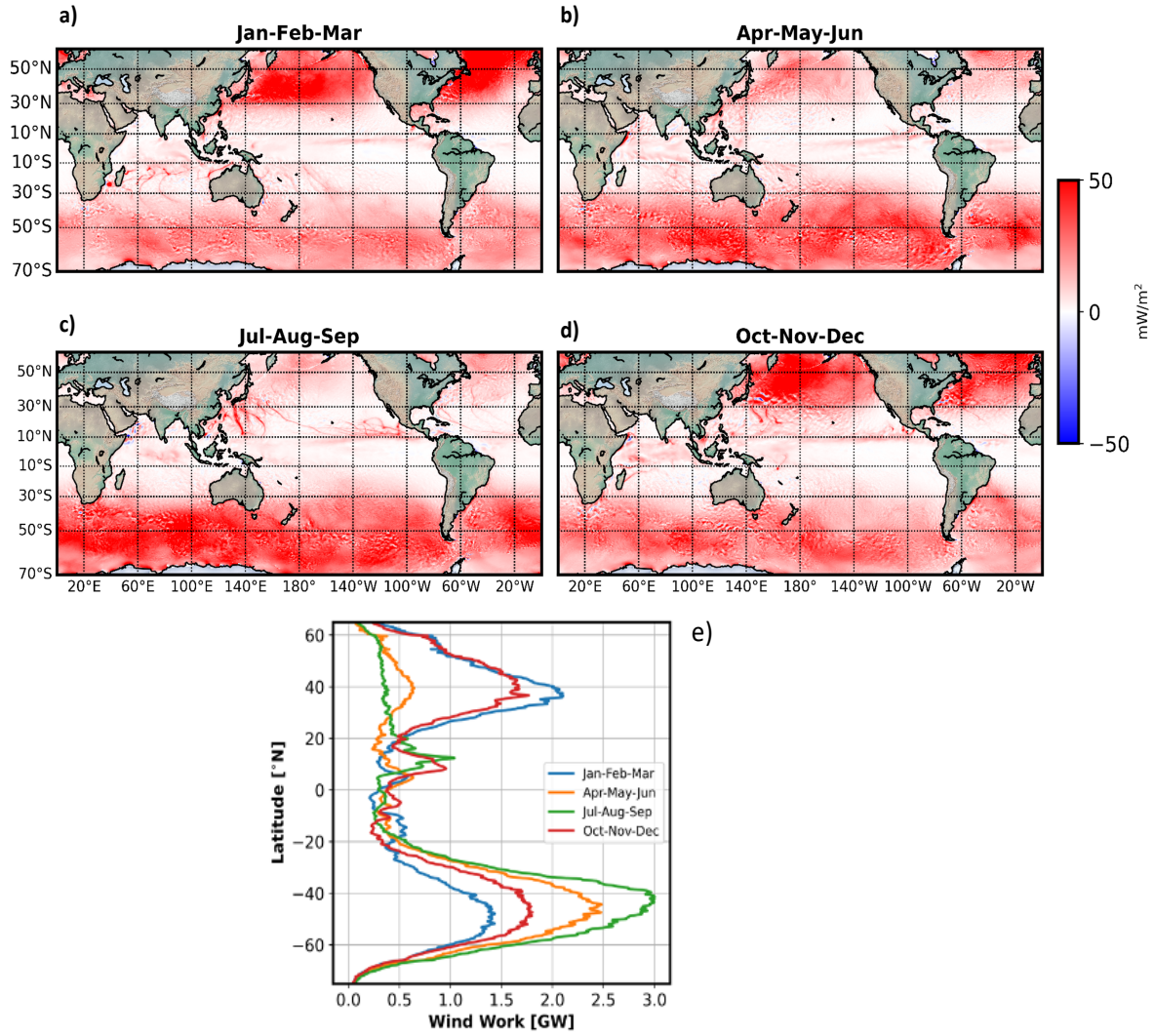
Figure 5. (a)–(d): Time-dependent component of the wind work, $\overline{\tau'.\mathbf{u_o}'}$, at different seasons. (e) wind work multiplied by the area of the numerical grid-cell (m^2) and zonally integrated during four seasons.
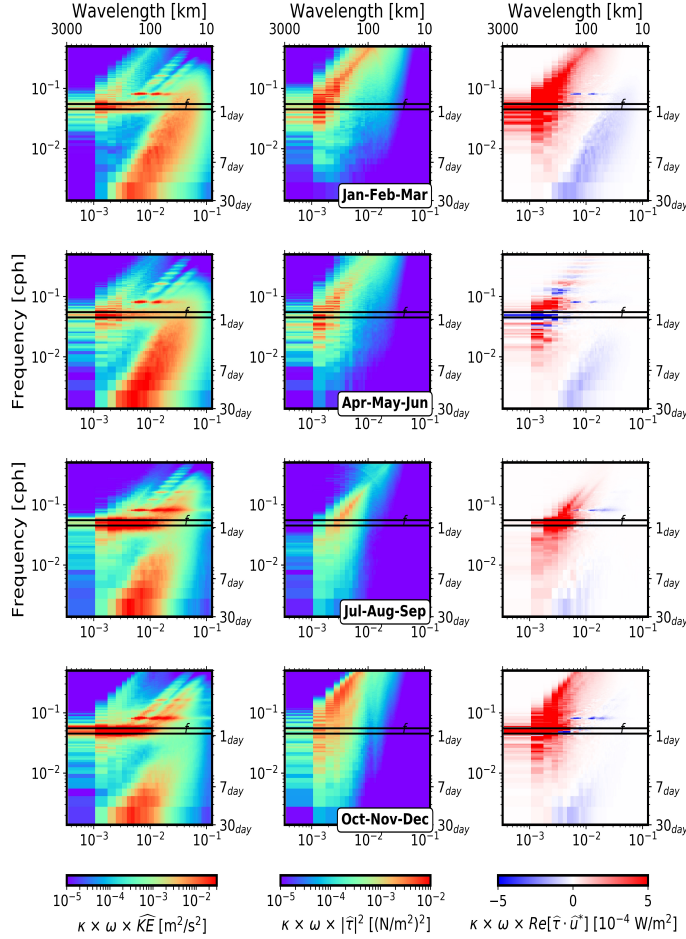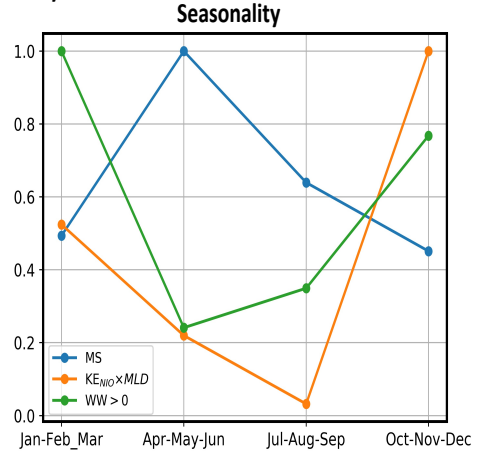
Figure 6. (a) Seasonal variability of the frequency-wavenumber spectra of surface current (first column), wind stress (middle column), and co-spectrum of the wind work. (b) Seasonal variability of kinetic energy associated to mesoscale motions, MS (defined by 350 km > L > 30 km and periods 30 days > T > 5 days, blue curve), kinetic energy of near-inertial motions times the mixed layer depth (orange curve), and positive wind work (green curve). The variance has been integrated then normalized by its maximum value.

summer. Wind work in tropical and equatorial regions has the same order of magnitude as the wind work at mid-latitudes.

In all seasons, wind work in tropical and equatorial latitudes, i.e. between $30°N$ and $30°S$, displays several zonal patterns elongated over ~ 3000 km mostly across the Indian, Pacific and Atlantic oceans with an intensification across the equator (Figures 4a–d). Such wind work, known to be associated with westward trade winds, impacts tropical and equatorial zonal jets (Maximenko et al., 2008; Chelton et al., 2011; Laurindo et al., 2017). The negative zonal band around $6°N$ is associated with the well-known eastward equatorial jet (Qiu et al., 2017). At these latitudes, wind work experiences a strong seasonality (Figures 4a–d) because of the trade winds seasonality across the equator. Wind work is also intensified south of $30°S$, i.e. in the Antarctic Circumpolar Current (ACC), for instance around the longitude of $130°E$, displaying elongated mesoscale patterns (100–400 km). These elongated mesoscale patterns are usually explained as the signature of the wind stress forcing on stationary mesoscale eddies trapped by topography as well as on eddies propagating eastward (Maximenko et al., 2008). Wind work at these southern mid-latitudes exhibits a weak seasonality because of the weak seasonality of the mean wind stress. However, wind work at northern mid-latitudes (north of $30°N$) exhibits a significant seasonality (Figure 4e) as well, as zonally elongated patterns at mesoscale (100–400 km) (Figure 4c) explained as the wind stress interacting with on zonally propagating eddies in western boundary currents (WBCs) (Maximenko et al., 2008; Chelton et al., 2011). The small wind work observed in summer at northern mid-latitudes is due to weak summertime wind stresses off the west coast of Asia and America that weakly impact mesoscale eddies within WBCs.

4.2 Total time-dependent component of the wind work: $\overline{\tau'.u_o'}$

The total time-dependent component of the wind work (Figures 5), that comprises the last three terms in eq. 4, differs from that of the time-mean wind work (Figures 4). The total time-dependent component is much weaker in tropical and equatorial regions (by a factor up to 3) and there is a strong seasonality in the southern hemisphere (compare Figure 5e and Figure 4e). In each hemisphere, at mid-latitudes ($>30°N$ and $<30°S$), wind work is large in fall and winter (Figures 5a,d (b,c) in the northern (southern) hemisphere) and smaller in spring and summer (Figures 5b,c (a,d) in the northern (southern) hemisphere). This is confirmed by the zonally averaged wind work (panel e). This seasonality at mid-latitudes is explained by synoptic atmospheric storms (with time scales of a few days) that are intensified in winter. These characteristics are consistent with previous studies (Watanabe and Hibiya, 2002; Zhai, 2013; Yu et al., 2018). Also, the emergence of hurricanes in summer and fall, in particular in the northern hemisphere, have a strong signature on the wind work (see for example Figure 5c, and also movies in Supporting Information).

Spectra of ocean current and wind stress for different seasons (respectively first and second columns of Figure 6a) in the Kuroshio Extension reveal how the different time and spatial scales associated with the wind work components vary seasonally. The effective spatial scales considered in these spectra are smaller than 1000 km and time scales smaller than three months. Within this time and spatial domain, ocean motions are dominated by near-inertial and higher frequency motions as well as by

lower frequency mesoscale eddies (<500 km). Currents with larger scales are weakly energetic in this region. The wind stress is found to be much weaker in spring and summer than in fall and winter. During fall and winter the wind stress has greater energy at higher frequencies (Figure 6a, second column). High-frequency ocean currents, such as near-inertial oscillations (NIO) forced by the wind stress, exhibit a seasonality different from the wind stress: NIOs are energetic in summer and fall (third and fourth rows on Figure 6a, first column) and weaker during winter and spring (first and second rows on Figure 6a, first column). One explanation is that wind stress forces NIO kinetic energy integrated over the mixed-layer depth. Since the mixed-layer depth is smaller in summer than in winter, the velocities associated with the total mixed layer NIO kinetic energy are larger in summer. This is confirmed when the surface NIO kinetic energy is multiplied by the mixed-layer depth: we recover a seasonality close to that of wind field and therefore of the wind work, as displayed on Figure 6b. Ocean currents with low-frequency, such as mesoscale eddies (with sizes larger than 100 km) and submesoscale structures, are less energetic in summer and fall compared with winter and spring (see Figure 6b). Such seasonality of low-frequency ocean motions is consistent with previous studies (Sasaki et al., 2014; Qiu et al., 2018; Callies et al., 2015; Rocha et al., 2016). Indeed, submesoscales (<50 km) become energetic in winter when the mixed-layer depth is large, with the kinetic energy of these scales being transferred to mesoscale eddies through the so-called inverse kinetic energy cascade, leading to higher mesoscale kinetic energy in spring (Sasaki et al., 2014; Lawrence and Callies, 2022).

From these wind work co-spectra, the total wind work is larger in fall and winter and smaller in spring and summer (Figure 6b), consistent with Figures 5. As illustrated on Figure 6a (last column), the time-dependent wind work is mostly explained by the component that forces near-inertial motions and in particular by the magnitude of the wind stress. The part that forces mesoscale eddies and submesoscales, i.e. motions with lower frequency, is negative with a much smaller magnitude. This component is further discussed in the next section.

4.3   Low-frequency component of the wind work: $\overline{\tau'_{lf}.\mathbf{u'_{o_{lf}}}} = \overline{\tau'_{lf>}.\mathbf{u'_{o_{lf>}}}} + \overline{\tau'_{lf<}.\mathbf{u'_{o_{lf<}}}}$

We now examine the low-frequency component of the wind work corresponding to wind stresses and ocean currents with periods larger than 3 days. Low-frequency ocean currents at mid-latitudes are often referred to as currents in geostrophic balance (balance between Coriolis and pressure gradients terms in the momentum equations), usually diagnosed from satellite altimetry (Chelton et al., 2011). The present numerical study includes, in addition, ageostrophic low-frequency currents (departing from geostrophy) that comprise ageostrophic eddy currents and surface wind-driven Ekman flow. These ageostrophic currents can explain 30 to 50 % of the total low-frequency currents in energetic areas (Qiu et al., 2014; Chassignet and Xu, 2017). However, we expect the correlation between wind stress and wind-driven Ekman flow to be larger than the correlation between wind stress and total eddy currents since the latter are mostly driven by the ocean interior dynamics.

Referring to Eq. 4, the low-frequency component is decomposed into two parts using a critical length scale, L_c: the first part, $\overline{\tau'_{lf>}.\mathbf{u'_{o_{lf>}}}}$), corresponds to wind stresses and ocean currents with spatial scales larger than L_c and the other one, $\overline{\tau'_{lf<}.\mathbf{u'_{o_{lf<}}}}$,
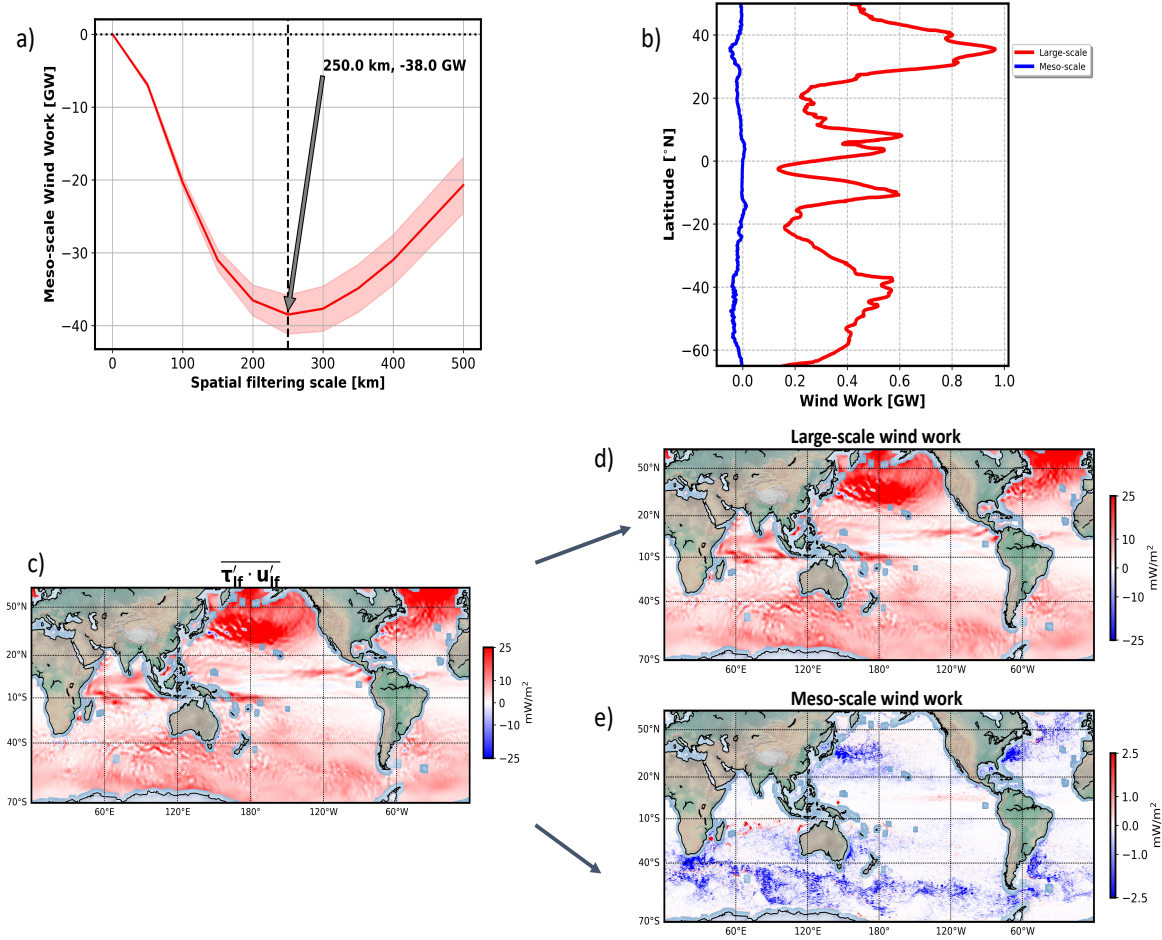
Figure 7. Low-frequency wind work. (a) Partition into positive and negative wind work. L_c is defined as the minimum of the blue (COAS) (see Rai et al. (2021) for the calculation of these curves) using 12 month outputs of wind stresses and ocean currents. Interpretation of L_c is that all wind work with scales smaller (larger) than L_c is negative (positive). (b) Zonally integrated low-frequency wind work with scales larger (red curve) and smaller (blue curve) than L_c from COAS during the period April-May-June. (c,d,e) Distribution in physical space of the wind work from COAS for scales larger (d) and smaller (e) than L_c during the period April-May-June.
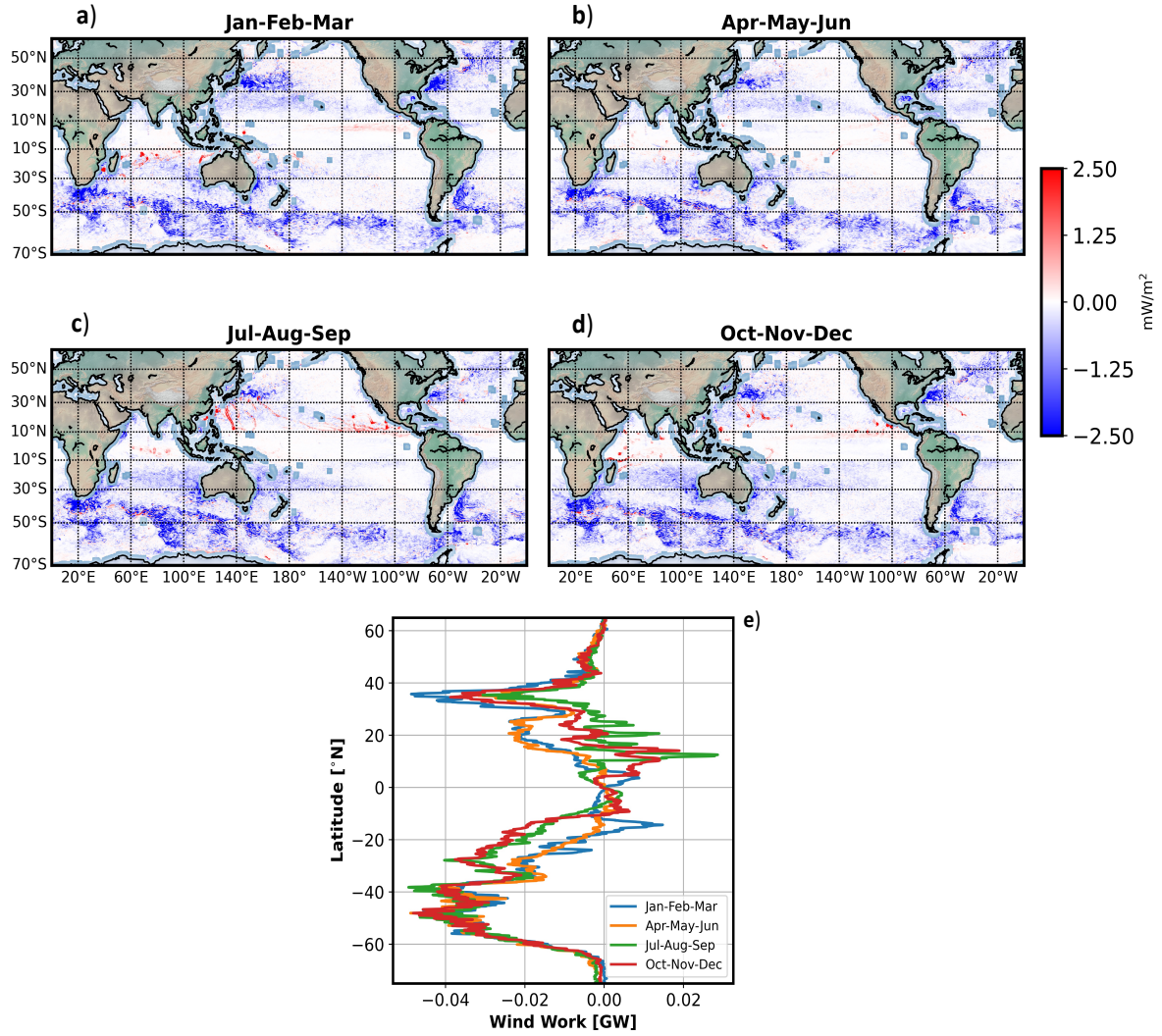
Figure 8. (a)–(d): Low-frequency wind work with scales smaller than L_c averaged over a period of 3 months, $\overline{\tau'_{lf<}\cdot\mathbf{uo}'_{lf<}}$. (e): wind work multiplied by the area of the numerical grid-cell (m^2) and zonally integrated during four seasons.
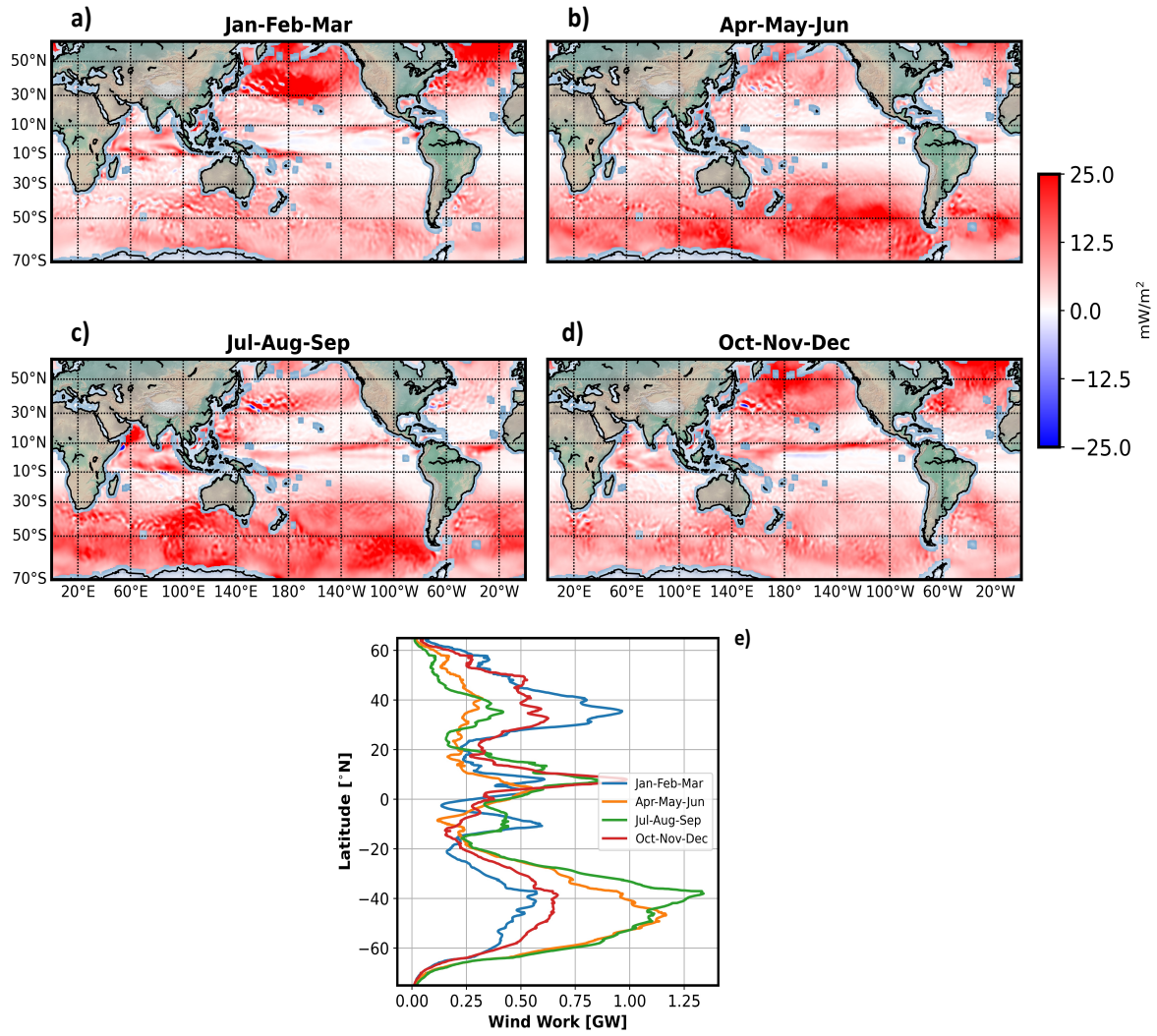
Figure 9. (a)–(d): Low-frequency wind work with scales larger than L_c averaged over a period of 3 months, $\overline{\tau'_{lf>}.\mathbf{uo}'_{lf>}}$. (e): wind work multiplied by the area of the numerical grid-cell (m^2) and zonally integrated during four seasons.

285   corresponding to wind stresses and ocean currents with scales smaller than L_c. The value, L_c, is defined such that the low-frequency component to the wind work is negative for scales smaller than L_c and positive for larger scales. The methodology to determine L_c follows Rai et al. (2021). The low-frequency fields ($\mathbf{X}'_{lf} = \boldsymbol{\tau}'_{\mathbf{lf}}$ or $\mathbf{u_o}'_{\mathbf{lf}}$) are convolved with a window function $\mathbf{G}_>$ (Top-Hat kernel to define the low-frequency component with spatial scales larger than L_c: $\mathbf{X}'_{lf>} = \mathbf{G}_> * \mathbf{X}'_{lf}$, where $*$ is a convolution on a sphere as described in Aluie (2019). Then, the low-frequency component to the wind work of all spatial

290   scales smaller than a given scale, L, has been estimated for the global ocean using 12 month outputs of wind stresses and ocean currents and is shown on Figure 7a. As expected, the wind work is negative for small scales and reaches a minimum at $L = L_c$ equal to 250 km for COAS simulation. This means that wind work for $L < L_c$ is negative and becomes postive for $L > L_c$.

   From Figures 8a–d, $\overline{\boldsymbol{\tau}'_{lf<}.\mathbf{u_o}'_{lf<}}$ (the wind work corresponding to scales $< L_c$) is negative in all seasons in most oceanic

295   regions. This points to the eddy damping effect explained by many studies (Eden and Dietze, 2009; Renault et al., 2016, 2018; Rai et al., 2021). An heuristic argument is that winds usually have scales larger than 500 km and therefore an approximation of the wind stress and wind work at small scales ($L < L_c$) is given by (using Eqs. 1 and 2):

$$\boldsymbol{\tau}'_{lf<} \approx \rho_{air}C_d|U_a|(-\mathbf{u_o}'_{lf<}), \tag{7}$$

$$\overline{\boldsymbol{\tau}'_{lf<}.\mathbf{u_o}'_{lf<}} \approx -\rho_{air}C_d\overline{|U_a||\mathbf{u_o}'_{lf<}|^2} < 0 \tag{8}$$

300   More detailed arguments are found in Renault et al. (2017) and Rai et al. (2021). From Figures 8a–d, the negative contribution of $\overline{\boldsymbol{\tau}'_{lf<}.\mathbf{u_o}'_{lf<}}$ is found principally at mid-latitudes in regions of energetic mesoscale eddies, such as the ACC and WBCs. Noticeably, this mid-latitude contribution does not vary seasonally as confirmed by the zonally integrated wind work (Figure 8e). Its magnitude is not large enough to impact the total time-dependent wind work (Figure 5e). In tropical and equatorial regions, a seasonality is observed (Figure 8e) even revealing small regions with positive wind work. Such

305   positive wind work cannot be explained by the arguments leading to Eq. 8. A closer look at Figures 8a–d and at movies (https://doi.org/10.5281/zenodo.6478679, in particular see the movie $GEOS\_ECCO\_TAUSPEED.mp4$) indicates that this positive wind work comes from the signature of hurricanes with a size smaller than L_c during summer and fall. However, this positive wind work has a much smaller magnitude than the negative wind work observed at mid-latitudes (Figure 7e).

310   Comparison of Figures 9a–d and 8a–d reveals that $\overline{\boldsymbol{\tau}'_{lf>}\mathbf{u_o}'_{lf>}}$ (the wind work corresponding to scales $> L_c$) much differs from $\overline{\boldsymbol{\tau}'_{lf<}.\mathbf{u_o}'_{lf<}}$, not only in terms of sign but also in terms in terms of magnitude and seasonality. These figures indicate that magnitude of $\overline{\boldsymbol{\tau}'_{lf>}\mathbf{u_o}'_{lf>}}$ is 10 times larger than $\overline{\boldsymbol{\tau}'_{lf<}.\mathbf{u_o}'_{lf<}}$ and is closer to, although smaller by a factor 2 than, the total time-dependent wind work (Figures 5e and 9e). The strong seasonality of $\overline{\boldsymbol{\tau}'_{lf>}\mathbf{u_o}'_{lf>}}$ resembles the total time-dependent wind work. These results indicate that the total time-dependent wind work at mid-latitudes splits almost equally into high-frequency and

315   low-frequency components. In tropical and equatorial regions, a comparison between Figures 5e and 9e reveals that patterns have a comparable magnitude, indicating that the high-frequency component of the wind work is small at these latitudes. The positive contribution of $\overline{\boldsymbol{\tau}'_{lf>}\mathbf{u_o}'_{lf>}}$, at mid-latitudes, should strengthen large-scale low-frequency ocean currents. As emphasized by Chen et al. (2014) and Yang et al. (2021), shear and baroclinic instabilities of these large-scale currents may generate

smaller-scale eddy currents. This suggests that production of smaller-scale eddies ($L < L_c$) by the positive part, $\overline{\tau'_{lf>}.\mathbf{u_o}'_{lf>}}$,

320 through instabilities, may be larger than the eddy damping as discussed in Section 3.2. This points to the importance of accounting for all wind work components to better infer the wind forcing of the ocean dynamics. The result also emphasizes that a full kinetic energy budget should account for all the wind work components as well as the nonlinear advection terms in the momentum equations, since the instabilities mentioned before are explained by these terms.

325 ### 4.4 High-frequency component of the wind work: $\overline{\tau'_{hf}.\mathbf{u_o}'_{hf}}$

From Eq. 4, the high-frequency component of the wind work is just the difference between the total time-dependent component (Figure 5e) and the low-frequency component, the latter being dominated by the large-scale component (Figure 9e). high-frequency and low-frequency components are dominant at mid-latitudes, i.e. at the location of atmospheric storm tracks, and have similar magnitudes as noted in the previous section. High-frequency winds are expected to force ocean currents prin-

330 cipally at the inertial frequency since the ocean is an oscillator with the frequency f. A strong forcing means that near-inertial motions should be in phase with wind stresses (Klein et al., 2004; Alford et al., 2016). To diagnose the phase relationship between high-frequency wind stresses and near-inertial and higher frequency ocean motions, we have re-estimated in the global ocean the total time-dependent component of the wind work by applying a phase lag between wind stresses and currents of 12 hours. Results (not shown) indicate that the resulting high-frequency component is reduced by a factor close to 10 at

335 mid-latitudes when integrated zonally in both hemispheres, with the new total time-dependent component now close to the low-frequency component. This result highlights wind stresses and ocean currents are largely in phase at short time scales.

To further understand the impact of high-frequency wind stress on the wind work, we have tested this phase relationship in spectral space, focusing on the Kuroshio Extension region. Figure 10a shows the wind work co-spectrum estimated from the

340 coupled simulation. As expected, the co-spectrum reveals a positive maximum around the inertial and higher frequencies, which corresponds to the forcing of near-inertial and higher frequency motions (Klein et al., 2004; Alford et al., 2016). The magnitude of the wind work for these high frequencies (in terms of period, T <3 days) is 52 mW/m^2. For time scales larger than 3 days, the wind work is negative (Figure 10a). This is related to the mesoscale eddy damping mentioned before, since low-frequency ocean motions in the Kuroshio Extension are mostly associated with mesoscale eddies and not large-scale currents. In terms of

345 negative wind work, the magnitude is -16 mW/m^2. Considering positive and negative wind work, the net wind-work is positive and equal to 36 mW/m^2. Similar results have been found in other areas of the world ocean, such as the ACC, the Gulf Stream and tropical regions (see Figure 11). We repeated this spectral calculation by applying a phase lag of 12 hours between wind stresses and ocean currents. Results (see the comparison of Figures 10a and b) indicate that the 12-hour offset impacts the wind work in the high-frequency band. In this spectral band, the wind work now displays alternating positive and negative

350 values. The wind work that impacts low frequency motions is almost unchanged by the offset. As a result the total wind work is slightly negative. Similar results (not shown) are obtained using a 3-hour or 6-hour offset. This test emphasizes not only the
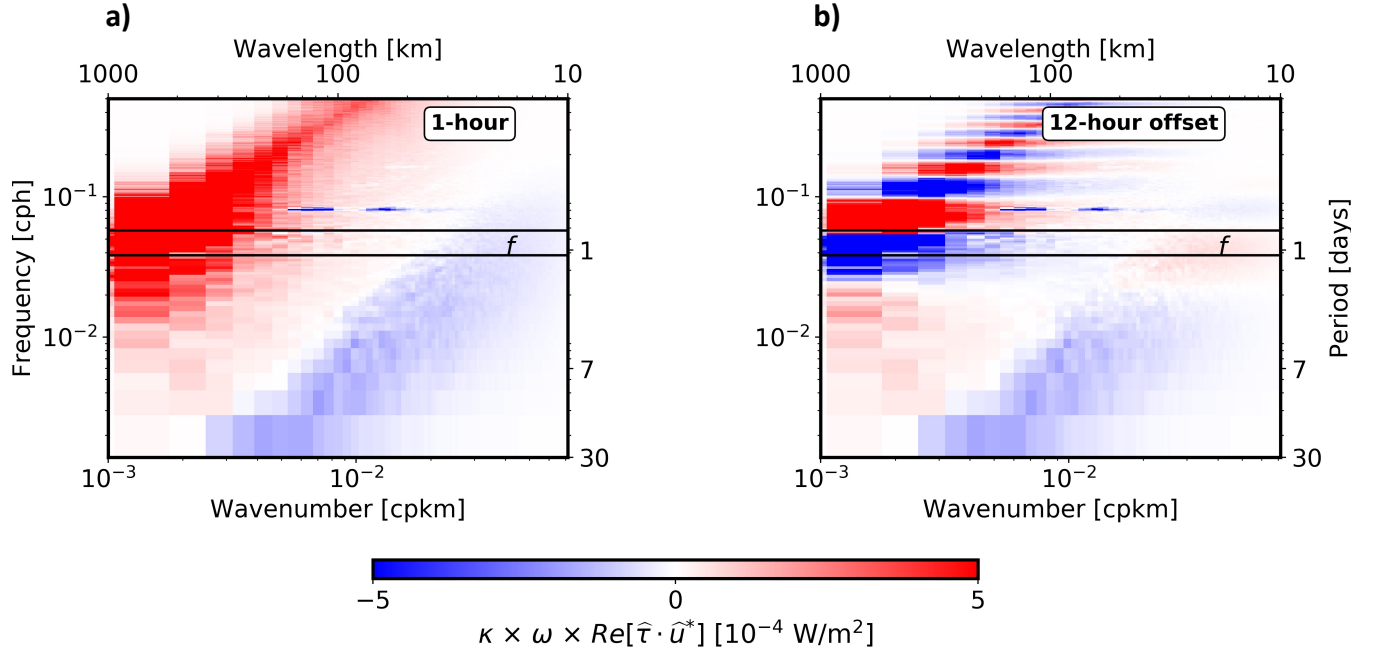
Figure 10. (a) co-spectrum of wind stresses and surface ocean currents in the Kuroshio Extension region from COAS simulation. (b) same as (a) except by offsetting wind stresses and surface currents by 12 hours. Using different offsettings (3 hours and 6 hours) produce the same results at 12 hours.

spatial collocation of wind stress and currents, but also their contemporaneity, which has an impact on the integrated wind work.

5   Discussion and Conclusion

The scalar product of wind stress and ocean surface current, called wind work, is the kinetic energy transfer between ocean and atmosphere. Our study has examined the impact of the wind work on the forcing of ocean currents using outputs of wind stresses and currents from a new coupled ocean-atmosphere simulation with high spatial resolution. Resulting wind stresses and surface ocean currents involve a broad range of time and space scales, from one hour to one year and 10 km to more than 3000 km. Our examination makes use of a simple method that splits the wind work into three components. (i) The high-frequency component, corresponding to wind stress and ocean current with time scales less than 3 days, (ii) the low-frequency component, corresponding to wind stress and ocean current with time scales between 3 days and 3 months, and (iii) the time-mean, or seasonal-mean, component diagnosed from wind stress and ocean current averaged over 3 months. Each of these three components, when integrated over the world ocean, does not vary much with seasons and explains 28% of the total wind work for the first two and 44% for the third one. This leads to a total wind work larger than 5 TW, a value close to recent estimations
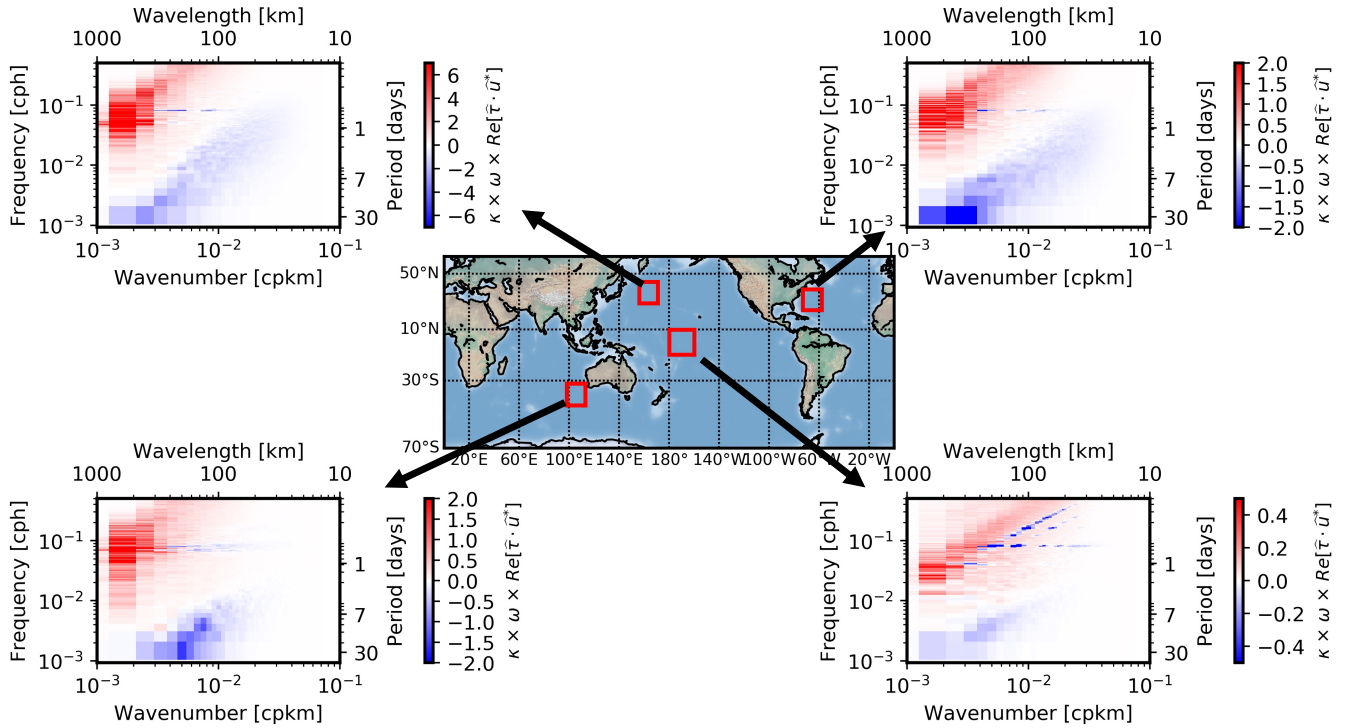
Figure 11. Co-spectrum of wind stresses and surface ocean currents in several regions from the COAS simulation (see square boxes in the middle panel). Note the color range is different in each panel.

365 (Yu et al., 2018; Yu and Metzger, 2019). However, the analysis in physical and spectral spaces of each of these components reveals a strong diversity their characteristics.

The high-frequency component of the wind work (time scales smaller than 3 days) dominates in regions of mid-latitude atmospheric storm tracks where it directly forces internal gravity waves, mostly near-inertial oscillations with large spatial scales.

370 One important characteristic of this component is its sensitivity to the phase relationship between wind stresses and ocean currents. Thus, a spectral analysis shows that a phase shift of 3 to 12 hours between wind stress and ocean current, reduces this component by a factor up to 10. The high frequency component also has a strong seasonality because of winter atmospheric storms .

375 The low-frequency component (corresponding to wind stress and ocean current with time scales between 3 days and 3 months) has been analyzed following Rai et al. (2021)'s approach which consists of defining a critical length scale that splits this component into a negative small-scale part and a positive large-scale part. The positive part exhibits a strong seasonality at mid-latitude, not present in the negative part. In addition, magnitude of the positive part is 10 times larger than the negative

part. These characteristics of the wind work, not found when using geostrophic currents diagnosed from altimetry datasets,
380   point to the importance of low-frequency ageostrophic current contribution to the wind work (Rai et al., 2021). The large
magnitude of the positive part may be explained by the strong correlation between wind stress and wind-driven Ekman flow.
Confirmation of this explanation will be the focus of a future study. The small-scale part acts as an eddy damping for mesoscale
eddies as discussed before (Eden and Dietze, 2009; Renault et al., 2016, 2018). This eddy damping effect may be counterbal-
anced by the positive large-scale part of the wind work. Indeed, instabilities of larger-scale currents may energize currents
385   associated with smaller eddies ($L < 250$ km). Reciprocally, smaller eddies can energize larger eddies through an inverse ki-
netic energy cascade. This emphasizes that the two low-frequency parts of the wind work cannot be examined separately, but
need to be examined through a full kinetic energy budget, a focus of a future work.

The time-mean, or seasonal-mean, component is significant in equatorial/tropical regions as well as at mid-latitudes. This com-
390   ponent forces equatorial and tropical zonal jets as well as stationary and propagating large eddies. It may also force tropical
wave instabilities, through nonlinear advection terms, but this has still to be assessed using a full kinetic budget as mentioned
before.

Our results emphasize the need to have satellite observations of wind stresses and currents, that are collocated and contempora-
395   neous, with a resolution of at least 10 km and a temporal resolution less than 12 hours. The present ASCAT wind observations
and ocean currents diagnosed from conventional altimeters do not meet these requirements. However, several future projects,
such as the wind and current mission (Odysea) (Rodríguez et al., 2019) and the Ocean Surface Current Multiscale Observa-
tion Mission (OSCOM) (Du et al., 2021), intend to address the limitations of existing wind stress and ocean current products.
Odysea mission aims to measure wind stresses and ocean surface currents (including both, geostrophic and ageostrophic cur-
400   rents) with sensors on-board a single satellite, with a spatial and temporal resolution of ~ 10 km and twice a day. In addition to
being collocated and contemporaneous, these global measurements of wind stress and ocean current will have wide-swaths, as
large as $\sim 1,800$ km. Observations from the upcoming Surface Water and Ocean Topography mission (SWOT) should allow
for the diagnosis of geostrophic currents with a resolution of $\sim$15 km over a wide-swath of 120 km (Fu and Ferrari, 2008;
Wang et al., 2019). Then, combining Odysea and SWOT observations should permit to assess the relative contributions of
405   geostrophic and ageostrophic currents to the wind work. We envision that these future observations, exploited in combination
with SST observations from Advanced Microwave Scanning Radiometer (AMSR-E), will permit estimates of not only the
kinetic energy budget (including the wind work and nonlinear advection of momentum), as suggested by the present study, but
also the heat budget in the upper ocean (Klein et al., 2019). Modelling studies like the present one should help to better assess
the potential of these missions.

410

Appendix A: Frequency-wavenumber spectrum and co-spectrum

The ω-κ spectrum of a given variable $\phi(x,y,t)$ is computed in a domain 1000 km-size and over 90 days. We refer the reader to Torres et al. (2018) for the full methodology. Briefly, before computing the ω-k spectrum of a $\phi(x,y,t)$, its linear trend is removed and a 3-D Hanning window is subsequently applied to the de-trended $\phi(x,y,t)$ (Qiu et al., 2018). A discrete 3-D Fourier transform is then computed to retrieve $\hat{\phi}(k,l,\omega)$ the Fourier coefficients, where $\hat{}$ is the Fourier transform, k the zonal wavenumber, l the meridional wavenumber, and ω the frequency. Finally, the 3-D Fourier transform is used to compute a 2-D spectral density, $|\hat{\phi}|^2(\kappa,\omega)$ where κ is the isotropic wavenumber defined as $\kappa = \sqrt{k^2 + l^2}$. The transformation from an anisotropic spectrum to an isotropic spectrum is performed following the methodology described by Torres et al. (2018).

The co-spectrum of the wind work is computed similarly to the ω-κ spectrum, following the methodology described in Flexas et al. (2019). First, the Fourier transforms of the wind stress $\hat{\tau}(k,l,\omega)$ and ocean current $\widehat{\mathbf{u_o}}(k,l,\omega)$ are calculated. The co-spectrum of the wind work is then given by

$$\widehat{F_s}(k,l,\omega) = Re\left[\widehat{\boldsymbol{\tau}.\mathbf{u_o}^*}(k,l,\omega)\right]$$

where Re is the real part of the complex quantity, and asterisk (*) the complex conjugate. The 2-D co-spectrum, $\widehat{\boldsymbol{\tau}.\mathbf{u_o}}(\kappa,\omega)$, is retrieved using the procedure described in the first paragraph of this appendix.

The ω-κ spectrum and co-spectrum are presented in a variance preserving form for easier comparison across the frequency-wavenumber domain.

Appendix B: Momentum budget in the upper oceanic layers

Let us assume a constant mixed-layer depth, H, for the sake of simplicity. Wind stress, $\boldsymbol{\tau}$, will force surface currents, $\mathbf{u_o}$, following

$$\frac{\partial \mathbf{u_o}}{\partial t} \sim \frac{\tau}{H} \tag{B1}$$

Using $\mathbf{u_o} = \overline{\mathbf{u_o}} + \mathbf{u_o}'$ and $\boldsymbol{\tau} = \overline{\boldsymbol{\tau}} + \tau'$, with overline being a time-average operator over 3.5 months, leads to

$$\frac{\partial \overline{\mathbf{u_o}} + \mathbf{u_o}'}{\partial t} \sim \frac{\overline{\boldsymbol{\tau}} + \tau'}{H} . \tag{B2}$$

Time-averaging Eq. B2 and multiplying the resulting equation by $\overline{\mathbf{u_o}}$ yields

$$\frac{\partial \overline{\mathbf{u_o}^2}/2}{\partial t} \sim \frac{\overline{\boldsymbol{\tau}}.\overline{\mathbf{u_o}}}{H} . \tag{B3}$$

After multiplying Eq. B2 by $\overline{\mathbf{u_o}} + \mathbf{u_o}'$ and taking the time average and using Eq. B3, we get

$$\frac{\partial \overline{\mathbf{u_o}'^2}/2}{\partial t} \sim \frac{\overline{\tau'.\mathbf{u_o}'}}{H} . \tag{B4}$$

The same operation can now be done using $\mathbf{u_o}' = \mathbf{u_o}_{hf}' + \mathbf{u_o}_{lf}'$, which leads to

$$\frac{\partial \overline{\mathbf{u_o}_{hf}'^2}/2}{\partial t} \sim \frac{\overline{\boldsymbol{\tau}'.\mathbf{u_o}_{hf}'}}{H} \ , \tag{B5}$$

$$\frac{\partial \overline{\mathbf{u_o}_{lf}'^2}/2}{\partial t} \sim \frac{\overline{\boldsymbol{\tau}'.\mathbf{u_o}_{lf}'}}{H} \ . \tag{B6}$$

The same arguments, but now in spatial space, can be applied using $\mathbf{u_o}_{lf}' = \mathbf{u_o}_{lf>}' + \mathbf{u_o}_{lf>}'$ leading to

$$\frac{\partial \overline{\mathbf{u_o}_{lf>}'^2}/2}{\partial t} \sim \frac{\overline{\boldsymbol{\tau}'.\mathbf{u_o}_{lf>}'}}{H} \ , \tag{B7}$$

$$\frac{\partial \overline{\mathbf{u_o}_{lf<}'^2}/2}{\partial t} \sim \frac{\overline{\boldsymbol{\tau}'.\mathbf{u_o}_{lf<}'}}{H} \ . \tag{B8}$$

Thus, from eqs. B3, B5, B6, B7, and B8, each term on the RHS of Eq. 4, related to a given fluctuation class, directly forces surface currents corresponding to the same class. Results above can also be understood if moving to the spectral space, since Eq. B1 becomes

$$\frac{\partial \widehat{\mathbf{u_o}}(\omega,k)}{\partial t} \sim \frac{\widehat{\tau}(\omega,k)}{H} \ . \tag{B9}$$

leading to

$$\frac{\partial |\widehat{\mathbf{u_o}}(\omega,k)|^2/2}{\partial t} \sim \frac{\Re[\widehat{\tau}(\omega,k).\widehat{\mathbf{u_o}}^*(\omega,k)]}{H} \ . \tag{B10}$$

with $\widehat{\ }$ the Fourier transform, * the conjugate, ω the frequency, k the wavenumber and $\mathcal{R}$ the real part. So, each frequency and each wavenumber of the wind stress forces surface currents with the same frequency and wavenumber.

However, the full momentum equations, including nonlinear advection terms, highlight that fluctuating wind stresses indirectly force mean surface currents and, similarly, mean wind stresses force fluctuating surface currents. These nonlinear effects are illustrated below.

Let us start with the full momentum equations

$$\frac{\partial \mathbf{u_o}}{\partial t} \sim -\mathbf{u_o} \cdot \nabla \mathbf{u_o} + \frac{\tau}{H} \ . \tag{B11}$$

Applying for example the decomposition $\mathbf{u_o} = \overline{\mathbf{u_o}} + \mathbf{u_o}'$ and $\boldsymbol{\tau} = \overline{\tau} + \tau'$ to Eq. B11 leads, after some calculations, to

$$\frac{\partial \overline{\mathbf{u_o}}^2/2}{\partial t} \sim -\overline{\mathbf{u_o}} \cdot \overline{\mathbf{u_o}} \cdot \nabla \overline{\mathbf{u_o}} - \overline{\mathbf{u_o}} \cdot \overline{\mathbf{u_o}' \cdot \nabla \mathbf{u_o}'} + \frac{\overline{\tau} \cdot \overline{\mathbf{u_o}}}{H} \ , \tag{B12}$$

$$\frac{\partial \overline{\mathbf{u_o}'^2}/2}{\partial t} \sim -\overline{\mathbf{u_o}' \cdot \mathbf{u_o}'} \cdot \nabla \overline{\mathbf{u_o}} - \overline{\mathbf{u_o}' \cdot \mathbf{u_o}' \cdot \nabla \mathbf{u_o}'} - \overline{\mathbf{u_o}} \cdot \overline{\mathbf{u_o}' \cdot \nabla \mathbf{u_o}'} + \frac{\overline{\tau'.\mathbf{u_o}'}}{H} \ . \tag{B13}$$

From eqs. B12 and B13, the time-mean and fluctuations surface currents, resulting directly from the wind work forcing, subsequently interact through the nonlinear advection terms in the momentum equations. For example, fluctuating surface

currents forced by wind stress fluctuations (Eq. B13) impact mean current through the second RHS term in Eq. B12. Similarly, mean current forced by mean wind stress (Eq.B12) impact current fluctuations through the first RHS term in Eq. B13 since these mean currents can be unstable. This example emphasizes that mean wind stress can force indirectly fluctuating currents and fluctuating wind stress can force indirectly mean currents. It confirms that the different components of the wind work displayed in Eq. 4 need to be considered altogether and not separately. Nonlinear interactions are more complex than shown in eqs. B12 and B13. This can be understood when moving again to the spectral space. Indeed, the generalization of Eq. B10 leads to

$$\frac{\partial |\widehat{\mathbf{u_o}}(\omega,k)|^2/2}{\partial t} \sim -\Re[(\widehat{\mathbf{u_o}.\nabla\mathbf{u_o}})(\omega,k).\widehat{\mathbf{u_o}}^*(\omega,k)] + \frac{\Re[\widehat{\tau}(\omega,k).\widehat{\mathbf{u_o}}^*(\omega,k)]}{H} . \tag{B14}$$

where $\mathbf{u_o}$ in the term $\widehat{\mathbf{u_o}.\nabla\mathbf{u_o}}(\omega,k)$ involve frequencies (ω_1 and ω_2) and wavenumbers (k_1 and k_2) such that $\omega_1 + \omega_2 = \omega$ and $k_1 + k_2 = k$.

Code availability. The exact version of the model used to produce the results used in this paper is archived on Zenodo (https://doi.org/10.5281/zenodo.6686083), as are input data and scripts to run the model and produce the plots.

Data availability. The coupled ocean-atmosphere simulation can be found at: https://portal.nccs.nasa.gov/datashare/G5NR/DYAMONDv2/GEOS_6km_Atmosphere-MITgcm_4km_Ocean-Coupled/GEOSgcm_output/. In particular, the dataset contained in the folder *geosgcm_surf/* were used in this study. The variables used in this study are U (east-west velocity component),V (north-south velocity component), oceTAUX (east-west wind stress component), and oceTAUY (north-south wind stress component).

Author contributions. HT and PK led the data analysis and data interpretation and drafted the manuscript. DM, CNH, AM, and ES helped develop and integrate the coupled ocean-atmosphere simulation. All authors contributed to the scientific interpretation of the results and reviewed the manuscript.

Competing interests. The authors declare that they have no conflict of interest.

Acknowledgements. This work was performed at the Jet Propulsion Laboratory, California Institute of Technology under prime contract with

485 NASA QuikSCAT project. Copyright 2021 California Institute of Technology. US government sponsorship acknowledged. HT, JW, AW, ER, DM, HZ, and DPM were supported by the NASA Physical Oceanography (PO) and Modeling, Analysis, and Prediction (MAP) programs. PK acknowledges support from the SWOT Science Team, the NASA S-Mode project and the QuikSCAT mission. AFT and MF were supported by the NASA S-MODE project and PDRDF funding from NASA's Jet Propulsion Laboratory BQ acknowledges support from NASA OSTST project. High-end computing was provided by the NASA Advanced Supercomputing (NAS) Division at the Ames Research Center.

References

Alford, M. H., MacKinnon, J. A., Simmons, H. L., and Nash, J. D.: Near-inertial internal gravity waves in the ocean, Annual review of marine science, 8, 95–123, 2016.

Aluie, H.: Convolutions on the sphere: commutation with differential operators, GEM - International Journal on Geomathematics, 10, 1–31, 2019.

Arbic, B. K., Alford, M. H., Ansong, J. K., Buijsman, M. C., Ciotti, R. B., Farrar, J. T., Hallberg, R. W., Henze, C. E., Hill, C. N., Luecke, C. A., Menemenlis, D., Metzger, E. J., Müeller, M., Nelson, A. D., Nelson, B. C., Ngodock, H. E., Ponte, R. M., Richman, J. G., Savage, A. C., Scott, R. B., Shriver, J. F., Simmons, H. L., Souopgui, I., Timko, P. G., Wallcraft, A. J., Zamudio, L., and Zhao, Z.: A Primer on Global Internal Tide and Internal Gravity Wave Continuum Modeling in HYCOM and MITgcm, in: New Frontiers in Operational Oceanography, edited by Chassignet, E. P., Pascual, A., Tintoré, J., and Verron, J., chap. 13, pp. 307–392, GODAE OceanView, https://doi.org/10.17125/gov2018.ch13, 2018.

Callies, J., Ferrari, R., Klymak, J. M., and Gula, J.: Seasonality in submesoscale turbulence, Nature communications, 6, 6862, 2015.

Chassignet, E. P. and Xu, X.: Impact of horizontal resolution (1/12 to 1/50) on Gulf Stream separation, penetration, and variability, Journal of Physical Oceanography, 47, 1999–2021, 2017.

Chelton, D. B., Schlax, M. G., and Samelson, R. M.: Global observations of nonlinear mesoscale eddies, Progress in Oceanography, 91, 167–216, 2011.

Chen, R., Flierl, G. R., and Wunsch, C.: A description of local and nonlocal eddy–mean flow interaction in a global eddy-permitting state estimate, Journal of Physical Oceanography, 44, 2336–2352, 2014.

Clarke, R.: Observational studies in the atmospheric boundary layer, Quarterly Journal of the Royal Meteorological Society, 96, 91–114, 1970.

Du, Y., Dong, X., Jiang, X., Zhang, Y., Zhu, D., Sun, Q., Wang, Z., Niu, X., Chen, W., Zhu, C., et al.: Ocean surface current multiscale observation mission (OSCOM): Simultaneous measurement of ocean surface current, vector wind, and temperature, Progress in Oceanography, 193, 102 531, 2021.

Eden, C. and Dietze, H.: Effects of mesoscale eddy/wind interactions on biological new production and eddy kinetic energy, Journal of Geophysical Research: Oceans, 114, 2009.

Ferrari, R. and Wunsch, C.: Ocean circulation kinetic energy: Reservoirs, sources, and sinks, Annual Review of Fluid Mechanics, 41, 2009.

Flexas, M. M., Thompson, A. F., Torres, H. S., Klein, P., Farrar, J. T., Zhang, H., and Menemenlis, D.: Global Estimates of the Energy Transfer From the Wind to the Ocean, With Emphasis on Near-Inertial Oscillations, Journal of Geophysical Research: Oceans, 124, 5723–5746, https://doi.org/10.1029/2018JC014453, 2019.

Fu, L.-L. and Ferrari, R.: Observing oceanic submesoscale processes from space, Eos, Transactions American Geophysical Union, 89, 488–488, 2008.

Garfinkel, C. I., Molod, A. M., Oman, L. D., and Song, I.-S.: Improvement of the GEOS-5 AGCM upon updating the air-sea roughness parameterization, Geophysical Research Letters, 38, n/a–n/a, https://doi.org/10.1029/2011GL048802, l18702, 2011.

Helfand, H. M. and Schubert, S. D.: Climatology of the Simulated Great Plains Low-Level Jet and Its Contribution to the Continental Moisture Budget of the United States, Journal of Climate, 8, 784–806, https://doi.org/10.1175/1520-0442(1995)008<0784:COTSGP>2.0.CO;2, 1995.

Klein, P., Lapeyre, G., and Large, W.: Wind ringing of the ocean in presence of mesoscale eddies, Geophysical research letters, 31, 2004.

Klein, P., Lapeyre, G., Siegelman, L., Qiu, B., Fu, L.-L., Torres, H., Su, Z., Menemenlis, D., and Le Gentil, S.: Ocean-Scale Interactions From Space, Earth and Space Science, 2019.

Komori, N., Ohfuchi, W., Taguchi, B., Sasaki, H., and Klein, P.: Deep ocean inertia-gravity waves simulated in a high-resolution global coupled atmosphere–ocean GCM, Geophysical research letters, 35, 2008.

Kondo, J.: Air-sea bulk transfer coefficients in diabatic conditions, Boundary-layer meteorology, 9, 91–112, 1975.

Large, W. and Pond, S.: Open ocean momentum flux measurements in moderate to strong winds, Journal of physical oceanography, 11, 324–336, 1981.

Large, W. G. and Yeager, S. G.: Diurnal to decadal global forcing for ocean and sea-ice models: The data sets and flux climatologies, NCAR Tech Note NCAR/TN-460+STR, Boulder, Colo. Natl. Cent. for Atmos. Res., 434, 2004.

Large, W. G., McWilliams, J. C., and Doney, S. C.: Oceanic vertical mixing: A review and a model with a nonlocal boundary layer parameterization, Reviews of Geophysics, 32, 363–403, 1994.

Laurindo, L. C., Mariano, A. J., and Lumpkin, R.: An improved near-surface velocity climatology for the global ocean from drifter observations, Deep Sea Research Part I: Oceanographic Research Papers, 124, 73–92, 2017.

Lawrence, A. and Callies, J.: Seasonality and spatial dependence of meso-and submesoscale ocean currents from along-track satellite altimetry, Journal of Physical Oceanography, 2022.

Maximenko, N. A., Bang, B., and Sasaki, H.: Observational evidence of alternating zonal jets in the world ocean, Geophysical research letters, 32, 2005.

Maximenko, N. A., Oleg V., M., Pearn P., N., and Hideharu, S.: Stationary mesoscale jet-like features in the ocean, Geophysical research letters, 35, 2008.

Molod, A., Suarez, M., and Partyka, G.: The impact of limiting ocean roughness on GEOS-5 AGCM tropical cyclone forecasts, Geophysical Research Letters, 40, 411–416, https://doi.org/10.1029/2012GL053979, 2013.

Molod, A., Takacs, L., Suarez, M., and Bacmeister, J.: Development of the GEOS-5 atmospheric general circulation model: evolution from MERRA to MERRA2, Geoscientific Model Development, 8, 1339–1356, https://doi.org/10.5194/gmd-8-1339-2015, 2015.

Nikurashin, M., Vallis, G. K., and Adcroft, A.: Routes to energy dissipation for geostrophic flows in the Southern Ocean, Nature Geoscience, 6, 48–51, 2013.

Panofsky, H. A., Tennekes, H., Lenschow, D. H., and Wyngaard, J.: The characteristics of turbulent velocity components in the surface layer under convective conditions, Boundary-Layer Meteorology, 11, 355–361, 1977.

Polzin, K. L. and Lvov, Y. V.: Toward regional characterizations of the oceanic internal wavefield, Reviews of geophysics, 49, 2011.

Qiu, B., Chen, S., Klein, P., Sasaki, H., and Sasai, Y.: Seasonal mesoscale and submesoscale eddy variability along the North Pacific Subtropical Countercurrent, Journal of Physical Oceanography, 44, 3079–3098, 2014.

Qiu, B., Nakano, T., Chen, S., and Klein, P.: Submesoscale transition from geostrophic flows to internal waves in the northwestern Pacific upper ocean, Nature Communications, 8, 1–10, 2017.

Qiu, B., Chen, S., Klein, P., Wang, J., Torres, H., Fu, L.-L., and Menemenlis, D.: Seasonality in transition scale from balanced to unbalanced motions in the world ocean, Journal of Physical Oceanography, 48, 591–605, 2018.

Rai, S., Hecht, M., Maltrud, M., and Aluie, H.: Scale of oceanic eddy killing by wind from global satellite observations, Science Advances, 7, eabf4920, https://doi.org/10.1126/sciadv.abf4920, 2021.

Renault, L., Molemaker, M. J., McWilliams, J. C., Shchepetkin, A. F., Lemarié, F., Chelton, D., Illig, S., and Hall, A.: Modulation of wind work by oceanic current interaction with the atmosphere, Journal of Physical Oceanography, 46, 1685–1704, 2016.

565 Renault, L., McWilliams, J. C., and Masson, S.: Satellite observations of imprint of oceanic current on wind stress by air-sea coupling, Scientific reports, 7, 1–7, 2017.

Renault, L., McWilliams, J., and Gula, J.: Dampening of Submesoscale Currents by Air-Sea Stress Coupling in the Californian Upwelling System, Scientific Reports, 8, 13 388, 2018.

Renault, L., Masson, S., Arsouze, T., Madec, G., and Mcwilliams, J. C.: Recipes for how to force oceanic model dynamics, Journal of
570 Advances in Modeling Earth Systems, 12, e2019MS001 715, 2020.

Rimac, A., von Storch, J.-S., Eden, C., and Haak, H.: The influence of high-resolution wind stress field on the power input to near-inertial motions in the ocean, Geophysical Research Letters, 40, 4882–4886, 2013.

Rocha, C. B., Gille, S. T., Chereskin, T. K., and Menemenlis, D.: Seasonality of submesoscale dynamics in the Kuroshio Extension, Geophysical Research Letters, 43, 11–304, 2016.

575 Rodríguez, E., Bourassa, M., Chelton, D., Farrar, J. T., Long, D., Perkovic-Martin, D., and Samelson, R.: The winds and currents mission concept, Frontiers in Marine Science, 6, 438, 2019.

Sasaki, H., Klein, P., Qiu, B., and Sasai, Y.: Impact of oceanic-scale interactions on the seasonal modulation of ocean dynamics by the atmosphere, Nature communications, 5, ncomms6636, 2014.

Stevens, B., Satoh, M., Auger, L., Biercamp, J., Bretherton, C. S., Chen, X., Düben, P., Judt, F., Khairoutdinov, M., Klocke, D., Kodama,
580 C., Kornblueh, L., Lin, S.-J., Neumann, P., Putman, W. M., Röber, N., Shibuya, R., Vanniere, B., Vidale, P. L., Wedi, N., and Zhou, L.: DYAMOND: the DYnamics of the Atmospheric general circulation Modeled On Non-hydrostatic Domains, Progress in Earth and Planetary Science, 6, 61, https://doi.org/10.1186/s40645-019-0304-z, 2019.

Strobach, E., Molod, A., Trayanov, A., Forget, G., Campin, J.-M., Hill, C., and Menemenlis, D.: Three-to-Six-Day Air–Sea Oscillation in Models and Observations, Geophysical Research Letters, 47, e2019GL085 837, https://doi.org/10.1029/2019GL085837, e2019GL085837
585 10.1029/2019GL085837, 2020.

Strobach, E., Klein, P., Molod, A., Fahad, A. A., Trayanov, A., Menemenlis, D., and Torres, H.: Local Air-Sea Interactions at Ocean Mesoscale and Submesoscale in a Western Boundary Current, Geophysical Research Letters, 49, 1–10, https://doi.org/10.1029/2021GL097003, 2022.

Su, Z., Wang, J., Klein, P., Thompson, A. F., and Menemenlis, D.: Ocean submesoscales as a key component of the global heat budget,
590 Nature communications, 9, 775, 2018.

Torres, H. S., Klein, P., Menemenlis, D., Qiu, B., Su, Z., Wang, J., Chen, S., and Fu, L.-L.: Partitioning ocean motions into balanced motions and internal gravity waves: A modeling study in anticipation of future space missions, Journal of Geophysical Research: Oceans, 123, 8084–8105, 2018.

Wang, J., Fu, L.-L., Torres, H., Chen, S., Qiu, B., and Menemenlis, D.: On the spatial scale to be resolved by the surface water and ocean
595 topography Ka-band fadar interferometer, Journal of Atmospheric and Oceanic Technology, 36, 87–99, 2019.

Watanabe, M. and Hibiya, T.: Global estimates of the wind-induced energy flux to inertial motions in the surface mixed layer, Geophysical research letters, 29, 64–1, 2002.

Yaglom, A. and Kader, B.: Heat and mass transfer between a rough wall and turbulent fluid flow at high Reynolds and Peclet numbers, Journal of Fluid Mechanics, 62, 601–623, 1974.

600 Yang, H., Wu, L., Chang, P., Qiu, B., Jing, Z., Zhang, Q., and Chen, Z.: Mesoscale Energy Balance and Air–Sea Interaction in the Kuroshio Extension: Low-Frequency versus High-Frequency Variability, Journal of Physical Oceanography, 51, 895–910, 2021.

Yu, Z. and Metzger, E. J.: The impact of ocean surface currents on global eddy kinetic energy via the wind stress formulation, Ocean Modelling, 139, 101 399, 2019.

Yu, Z., Fan, Y., Metzger, E. J., and Smedstad, O. M.: The wind work input into the global ocean revealed by a 17-year global HYbrid coordinate ocean model reanalysis, Ocean Modelling, 130, 29–39, 2018.

Zhai, X.: On the wind mechanical forcing of the ocean general circulation, Journal of Geophysical Research: Oceans, 118, 6561–6577, 2013.

Zhai, X.: Dependence of energy flux from the wind to surface inertial currents on the scale of atmospheric motions, Journal of Physical Oceanography, 47, 2711–2719, 2017.

Zhai, X., Johnson, H. L., Marshall, D. P., and Wunsch, C.: On the wind power input to the ocean general circulation, Journal of Physical Oceanography, 42, 1357–1365, 2012.